On the recovery of effective elastic thickness using spectral methods: Examples from synthetic data and from the Fennoscandian Shield

Marta Pérez-Gussinyé,[1] Anthony R. Lowry,[2] Anthony B. Watts,[1] and Isabella Velicogna[2]

Received 8 September 2003; revised 23 March 2004; accepted 12 May 2004; published 16 October 2004.

[1] There is considerable controversy regarding the long-term strength of continents (T_e). While some authors obtain both low and high T_e estimates from the Bouguer coherence and suggest that both crust and mantle contribute to lithospheric strength, others obtain estimates of only <25 km using the free-air admittance and suggest that the mantle is weak. At the root of this controversy is how accurately T_e can be recovered from coherence and admittance. We investigate this question by using synthetic topography and gravity anomaly data for which T_e is known. We show that the discrepancies stem from comparison of theoretical curves to multitaper power spectral estimates of free-air admittance. We reformulate the admittance method and show that it can recover synthetic T_e estimates similar to those recovered using coherence. In light of these results, we estimate T_e in Fennoscandia and obtain similar results using both techniques. T_e is 20–40 km in the Caledonides, 40–60 km in the Swedish Svecofennides, 40–60 km in the Kola peninsula, and 70–100 km in southern Karelia and Svecofennian central Finland. Independent rheological modeling, using a xenolith-controlled geotherm, predicts similar high T_e in central Finland. Because T_e exceeds crustal thickness in this area, the mantle must contribute significantly to the total strength. T_e in Fennoscandia increases with tectonic age, seismic lithosphere thickness, and decreasing heat flow, and low T_e correlates with frequent seismicity. However, in Proterozoic and Archean lithosphere the relationship of T_e to age is ambiguous, suggesting that compositional variations may influence the strength of continents. *INDEX TERMS:* 8159 Tectonophysics: Rheology—crust and lithosphere; 8164 Tectonophysics: Stresses—crust and lithosphere; 8122 Tectonophysics: Dynamics, gravity and tectonics; 8110 Tectonophysics: Continental tectonics—general (0905); *KEYWORDS:* effective elastic thickness Bouger coherence, free-air admittance synthetic data, Fennoscandian Shield seismicity

Citation: Pérez-Gussinyé, M., A. R. Lowry, A. B. Watts, and I. Velicogna (2004), On the recovery of effective elastic thickness using spectral methods: Examples from synthetic data and from the Fennoscandian Shield, *J. Geophys. Res.*, *109*, B10409, doi:10.1029/2003JB002788.

1. Introduction

[2] To understand how the lithosphere responds to loads on timescales $>10^5$ years, we parameterize its strength in terms of the effective thickness T_e of an idealized elastic beam that would bend by the same amount as the lithosphere under the same applied loads [e.g., *Watts*, 2001]. Because, in practice, the layers composing the lithosphere fail anelastically in both brittle and ductile fashion, T_e actually represents an integral of the bending stress within limits imposed by the rheology of the lithosphere [*Goetze and Evans*, 1979; *Burov and Diament*, 1995; *Brown and Phillips*, 2000]. Consequently, T_e depends on mineralogy, temperature, and state of stress of the lithosphere. Oceanic lithosphere, with a thin and mafic crust, generally behaves like a single mechanical layer. Oceanic mantle is relatively homogeneous, and the ocean geotherm is dominated by plate cooling, so T_e of oceanic lithosphere increases with thermal age of the lithosphere at the time of loading [*Watts*, 1978]. However, continental lithosphere is characterized by a much greater variation in composition, thermal state, and state of stress, such that a simple relationship between T_e and these parameters has not yet been established. Furthermore, the wide range of inverse methods and the loading assumptions used to estimate continental T_e yield very different results, even when the same data sets are used. This has generated considerable controversy regarding the actual values of T_e and their interpretation.

[3] Many estimates of continental T_e are derived using either the coherence function between topography and Bouguer gravity (here referred to as Bouguer coherence) or from the transfer function relating topography and free-air gravity (free-air admittance). The Bouguer coherence

[1]Department of Earth Sciences, Oxford University, Oxford, UK.
[2]Department of Physics, University of Colorado, Boulder, Colorado, USA.

0148-0227/04/2003JB002788$09.00

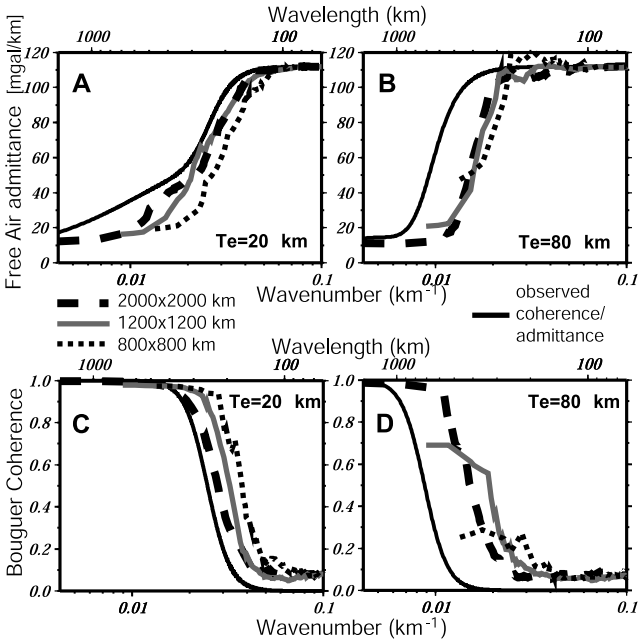

Figure 1. Theoretical (black line) and observed (gray and dashed black lines) (a, b) admittance and (c, d) coherence functions for T_e = 20 km (Figures 1a and 1c) and 80 km (Figures 1b and 1d). Observed coherence and admittance functions were calculated using windows of synthetic topography and gravity data of 2000 × 2000 km, 1200 × 1200 km, and 800 × 800 km (see legend).

measures the correlation of topography and Bouguer gravity data as a function of wavelength and is generally near zero at short wavelengths where loads are supported predominantly by stress [*Forsyth*, 1985]. At long wavelengths where loads are supported in an Airy-type fashion, the coherence approaches one (Figure 1). The free-air anomaly and hence the admittance tend to zero at long wavelengths and at short wavelengths approach a large value (Figure 1). Both the admittance and the coherence functions exhibit transitional behavior at intermediate wavelengths depending upon the strength of the lithosphere.

[4] Spectral methods for estimating T_e compare the observed spectral function to model predictions for a given elastic thickness. The resulting T_e estimates are very sensitive to assumptions about lithospheric loading. Early spectral studies [*Banks et al.*, 1977] modeled the admittance function assuming that all loading occurs as topographic masses emplaced atop the lithosphere. Such studies yielded very small T_e = 5–10 km for the continental United States [*Banks et al.*, 1977] and ~1 km for cratonic lithosphere of Australia [*McNutt and Parker*, 1978]. *Forsyth* [1985] noted that if models of Bouguer gravity admittance assume surface loading but mass anomalies within the lithosphere contribute some fraction of lithospheric loading, T_e will be underestimated. Subsurface loading can result, for example, from thermal processes that cool or heat the lithosphere, crustal underplating, or intracrustal thrusting during orogeny. *Forsyth* [1985] suggested that a flexural isostatic model must include both surface and subsurface loads in order to accurately estimate T_e. He also suggested that the Bouguer coherence more accurately estimates T_e since it is less sensitive than admittance to the ratio of subsurface to surface loading, f, which is unknown but can be estimated from the data if T_e is known.

[5] Since *Forsyth*'s [1985] study, most estimates of continental T_e have used either the Bouguer coherence function including surface and subsurface loads or forward modeling where loading processes are well understood. The results of these two techniques generally agree [e.g., *Armstrong and Watts*, 2001] and indicate that continental lithosphere can be both very weak and very strong [e.g., *Watts*, 2001]. These methods yield high T_e estimates of 60 to >100 km in cratonic interiors, much greater than the crustal thickness, suggesting that the mantle is strong in these areas [e.g., *Poudjom Djomani et al.*, 1999; *Bechtel et al.*, 1989; *Wang and Mareschal*, 1999; *Hartley et al.*, 1996; *Petit and Ebinger*, 2000; *Kogan et al.*, 1994; *Swain and Kirby*, 2003a]. These methods also yield low estimates of T_e in areas of young tectonothermal age [e.g., *Watts*, 2001]. Intermediate T_e estimates in old lithosphere (e.g., the Tien Shan, age ~700 Ma, T_e < 25 km [*Burov et al.*, 1990] and the Carpathian foredeep, age ~1.6 Ga, T_e < 40 km [*Stewart and Watts*, 1997]) are thought to reflect decoupling of the crust and mantle by a weak, ductile lower crust [e.g., *Burov and Diament*, 1995; *Lavier and Steckler*, 1997; *Brown and Phillips*, 2000]. Independent evidence for a weak lower crust derives from experimental rock mechanics [*Brace and Kohlstedt*, 1980] and from the early observation that earthquakes occur mainly in the upper crust, some few in the upper mantle, but only rarely in the lower crust [*Chen and Molnar*, 1983].

[6] However, recent studies using improved relocation techniques have shown that some of these "deeper" earthquakes may occur in the lower crust rather than in the mantle [*Maggi et al.*, 2000]. Additionally, some authors have questioned high estimates of T_e derived from the Bouguer coherence method. *McKenzie* [2003] argues that particularly in ancient cratons, erosion and sedimentation reduce the topographic response to subsurface loads and decorrelate the topography with the gravity response to those loads. If this were the case, Bouguer coherence might overestimate T_e. *McKenzie* [2003] suggests that the free-air admittance can better estimate T_e since it uses only the portion of free-air gravity which is correlated with topography. *McKenzie*'s [2003] free-air admittance estimates of T_e < 25 km in continents are similar or smaller than the revised seismogenic thicknesses. Therefore *Maggi et al.* [2000] and *Jackson* [2002] suggest that the lithospheric strength resides in the upper and lower crust and the mantle is, in fact, weak.

[7] The relative strength of the crust and mantle has far-ranging implications for how we describe tectonic processes. At the core of this debate is the question of whether T_e estimates from the free-air admittance and Bouguer coherence accurately represent the true strength of the lithosphere. The purpose of this paper is to investigate the causes for discrepancies in estimates from these two techniques. For clarity, we organize the paper in two parts. In part 1 (sections 2 and 3) we use synthetic tests to examine spectral methods for T_e estimation. We first describe the methods used here to estimate T_e from multitaper spectral

estimates of free-air admittance and Bouguer coherence, including a reformulation of the free-air admittance to remove potential sensitivity to bias errors. We then evaluate how accurately the Bouguer coherence and free-air admittance methods recover known T_e structures (both uniform and spatially varying) from synthetic data. In light of these results, we estimate and interpret the T_e structure in Fennoscandia using both techniques in part 2 (sections 4–6) of the paper. We vary the size of the analysis windows to optimize the resolution/bias of recovered T_e, and we examine potential effects of noise due to postglacial rebound and long-term erosion in the free-air admittance and Bouguer coherence results. We also compare the admittance and coherence estimates of T_e in central Finland to rheological estimates of T_e using xenolith-derived geotherms. Finally, we examine the relationship of T_e to other parameters such as tectonic age, heat flow, seismic lithosphere thickness, and seismicity.

2. Part 1: T_e Estimation Using Spectral Methods

[8] Flexural isostasy assumes that loads are partly supported by stresses within the elastic lithosphere and partly by buoyancy anomalies generated by deflection of the lithosphere overlying a fluid asthenosphere [*Gunn*, 1943]. The relative importance of stress versus flexural deflection in compensating loads at a given wavelength depends on the flexural rigidity of the elastic plate, D:

$$D = \frac{ET_e^3}{12(1-\sigma^2)}, \tag{1}$$

where E is Young's modulus and σ is Poisson's ratio (parameters used in this paper are given in Table 1). A large elastic thickness corresponds to a strong lithosphere in which elastic stress supports a significant fraction of loading and the lithosphere resists flexure. A small elastic thickness implies relatively little elastic support of stress.

[9] We estimate T_e using both Bouguer coherence and free-air admittance. In each case, we first calculate the observed coherence/admittance and then compare it to coherence/admittance predicted for a range of T_e values. Surface and subsurface loads are deconvolved from the data for a given T_e, and coherence/admittance are then calculated assuming that the loads are statistically uncorrelated [*Forsyth*, 1985]. The best fit T_e estimate is that which yields a minimum root-mean-square error between the observed and predicted coherence or admittance.

[10] The observed Bouguer coherence is a measure of the degree to which Bouguer gravity can be linearly predicted from topography (or vice versa) and is given by

$$\gamma^2_{\text{obs}}(k) = \left\langle \frac{|S_{hb}(\mathbf{k})|^2}{S_{hh}(\mathbf{k})S_{bb}(\mathbf{k})} \right\rangle, \tag{2}$$

where S_{hb} is the multitaper estimate of the cross-power spectrum of Bouguer gravity and topography and S_{hh} and S_{bb} are the multitaper estimates of the autopower spectra of topography and gravity, respectively. Angle brackets denote averaging over annular wave number bins, $\mathbf{k}$ is the two-dimensional wave number vector, and $k = |\mathbf{k}| = \sqrt{\mathbf{k}_x^2 + \mathbf{k}_y^2}$.

Table 1. Parameters Used to Generate the Synthetic Data

Parameter	Symbol	Value	Units
Crustal density	ρ_c	2.67	g cm^{-3}
Mantle density	ρ_m	3.3	g cm^{-3}
Crustal thickness	z_c	40	km
Young modulus	E	10^{11}	Pa
Poisson's ratio	σ	0.25	

The observed free-air admittance, $Z(\mathbf{k})$, is the linear transfer function

$$Z_{\text{obs}}(k) = \frac{\langle S_{fh}(\mathbf{k}) \rangle}{\langle S_{hh}(\mathbf{k}) \rangle}, \tag{3}$$

where S_{hf} is the cross-power spectrum of topography and free-air gravity.

[11] Several different spectral estimators have been applied to estimate coherence and admittance in T_e studies. In this paper we use a multitaper spectral estimation technique [*Thomson*, 1982]. The multitaper method tapers (or windows) the data with a set of orthogonal functions. In this study we use discrete prolate-spheroidal sequences [*Slepian*, 1978]. The final, minimum bias spectrum at each wave number (k_x, k_y) is a weighted average of the spectra generated for each of the individual tapers. The multitaper estimator reduces the variance of the spectral estimate and also defines spectral resolution [*Percival and Walden*, 1993]. Tests with synthetic data show that the multitaper estimator allows a more accurate T_e recovery than the periodogram method (i.e., spectral estimation in which no taper is applied to the data) or a simple Hanning taper [e.g., *Ojeda and Whitman*, 2002].

[12] Typically, estimates of coherence and admittance use power spectra averaged over a range of two-dimensional wave numbers to reduce the variance in spectral estimates. *Simons et al.* [2000] discuss a variety of such averaging methods. In principal, there is no need for spectral domain averaging of multitaper spectra because the weighted average of individual tapers already serves the purpose of smoothing the solution to stabilize it [e.g., *Swain and Kirby*, 2003b]. However, our synthetic tests indicate that averaging in annular wave number bins to generate a one-dimensional admittance or coherence function greatly reduces the variance in the resulting estimates of T_e relative those obtained from two-dimensional coherence and admittance functions as in the work by *Swain and Kirby* [2003b], although this neglects possible anisotropy of the isostatic response. Hence, in all analyses presented here the coherence and admittance functions have been reduced to one dimension by averaging within annular wave number bins.

[13] We form the predicted coherence and admittance functions from the topography and gravity data. For the Bouguer coherence we follow the method outlined by *Lowry and Smith* [1994] and *Forsyth* [1985]. We also reformulate the predicted free-air admittance so that it is calculated in a manner consistent with the Bouguer coherence. First, we use the observed topography and Bouguer or free-air gravity anomaly to solve for the surface and internal loads, using relations given in Appendix A and an assumed elastic thickness T_e. Second, we calculate components of the topography and Bouguer and free-air gravity due to surface

loading, H_t, B_t, and F_t, and subsurface loading, H_b, B_b, and F_b. If surface and subsurface loads are statistically uncorrelated, all cross-power spectra involving a surface load contribution and a subsurface load contribution will have an expected value of zero. The recombination of these individual autopower and cross-power spectra, neglecting the $\mathcal{E}\{S\} = 0$ terms, yields a predicted coherence:

$$\gamma^2_{\text{pred}}(k) = \left\langle \frac{\left|S^{tt}_{hb}(\mathbf{k}) + S^{bb}_{hb}(\mathbf{k})\right|^2}{\left[S^{tt}_{hh}(\mathbf{k}) + S^{bb}_{hh}(\mathbf{k})\right]\left[S^{tt}_{bb}(\mathbf{k}) + S^{bb}_{bb}(\mathbf{k})\right]} \right\rangle, \quad (4)$$

where the superscripts indicate surface (t) or subsurface (b) loading components. Note that usually in equations (2) and (4) the numerator and denominator are first averaged in annular wave number bins and then the quotient is formed. Averaging after forming the quotient, as done here, was found to perform better in earlier synthetic tests using maximum entropy power spectra [*Lowry and Smith*, 1994] and yields similar results using the multitaper spectral estimator.

[14] Similarly, the predicted admittance function becomes

$$Z_{\text{pred}}(k) = \frac{\langle S^{tt}_{fh}(\mathbf{k}) + S^{bb}_{fh}(\mathbf{k})\rangle}{\langle S^{tt}_{hh}(\mathbf{k}) + S^{bb}_{hh}(\mathbf{k})\rangle}. \quad (5)$$

The best fit elastic thickness minimizes the weighted root-mean-square error:

$$\epsilon_\gamma = \sqrt{\frac{\sum_{i=1}^{N}\left[\gamma_{\text{obs}}(k_i) - \gamma_{\text{pred}}(k_i)\right]^2/\sigma^2_\gamma(k_i)}{\sum_{i=1}^{N} 1/\sigma^2_\gamma(k_i)}} \quad (6)$$

$$\epsilon_Z = \sqrt{\frac{\sum_{i=1}^{N}\left[Z_{\text{obs}}(k_i) - Z_{\text{pred}}(k_i)\right]^2/\sigma^2_Z(k_i)}{\sum_{i=1}^{N} 1/\sigma^2_Z(k_i)}}, \quad (7)$$

where N is the number of annular wave number bins and $\sigma^2_\gamma(k_i)$ and $\sigma^2_Z(k_i)$ are the variances of the observed coherence and admittance calculated via the jackknife method [*Thomson and Chave*, 1991] and averaged within annular bins. We find the best fit T_e from a search over a large range of possible estimates.

[15] It is important to note that both coherence and admittance depend on the loading ratio, f, as well as on T_e. Although coherence depends weakly on f relative to the strong f dependence of admittance [*Forsyth*, 1985], the solution is nonunique unless another piece of information is added. *Forsyth* [1985] suggested that minimization of the statistical correlation of surface and subsurface loads can provide this additional information. One can identify processes, such as coupled volcanic construction and thermal perturbation [e.g., *Macario et al.*, 1995] that may correlate surface and subsurface loads at a particular location and/or a narrow range of wave numbers. However, an incorrect choice of T_e in the calculations described in Appendix A will artificially correlate loads at all locations and all scales, such that minimization of load correlation can be expected to yield an optimal estimate of T_e even in the presence of correlated loads [*Lowry and Zhong*, 2003].

[16] If the observed and predicted coherence/admittance functions are calculated from the topography and gravity anomaly data using identical windowing and processing steps, we expect adequate recovery of T_e, provided noise processes (e.g., subsurface loads without surface expression, multiple depths of subsurface loading, correlated loads, anisotropy of the isostatic response) have minor effects. However, if the observed coherence/admittance are compared to purely theoretical coherence/admittance curves, which correspond to the solution for an infinitely large data window, erroneous results are expected (see section 3.1). All of the results presented in this paper use a multitaper windowing scheme with $NW = 3$, where N is the number of samples in the series and W is the half bandwidth of the central lobe of the power spectral density of the tapers [see, e.g., *Simons et al.*, 2000, Figure 2]. The choice of bandwidth parameter NW in the multitaper technique is important. As the bandwidth increases, the resolution (i.e., the minimum separation in wave number between approximately uncorrelated spectral estimates) decreases [*Walden et al.*, 1995]. For a given bandwidth, W, there are up to $k = 2NW - 1$ tapers with good leakage properties [*Percival and Walden*, 1993]. Variance of spectral estimates decreases with the number of tapers as $1/k$, so the bandwidth and resolution are chosen depending on the individual function under analysis [*Percival and Walden*, 1993]. We found that Bouguer coherence estimates of T_e are optimized using five tapers to construct the autopower and cross power spectra. However, T_e recovered from free-air admittance yielded better results using just the three lower-order tapers rather than using five tapers. This is probably because higher-order tapers have poorer leakage properties [*Percival and Walden*, 1993], coupled with the fact that admittance is more prone to leakage at wavelengths where isostatic compensation occurs because free-air gravity has low power at these wavelengths. In this paper the coherence and admittance functions were calculated using five and three tapers, respectively.

[17] Other elements of the deconvolution and signal processing are identical to those discussed by *Lowry and Smith* [1994], including deconvolution of the surface and subsurface load responses within a much larger data window (2048 × 2048 km) than the window in which power spectra are estimated, as recommended by *Lowry and Smith* [1994]. This approach differs from that used, e.g., by *Swain and Kirby* [2003a], who deconvolved loads in the same tapered windows as used to estimate multitaper power spectra. We found that the bias and variance of T_e estimates is greatly reduced by deconvolving in the larger window. Bias is introduced in small tapered windows for reasons which we discuss further in section 3.2.1.

3. Tests With Synthetic Gravity and Topography Data

3.1. Generation of Synthetic Gravity and Topography Data

[18] We generate synthetic topography and gravity data by placing uncorrelated surface and subsurface mass loads on an elastic plate using an algorithm similar to that of *Macario et al.* [1995]. Fourier amplitudes of the initial surface, $\mathcal{H}_i(k)$, and subsurface, $\mathcal{W}_i(k)$, loads were generated

so that their power spectra mimics that of actual topography. For this we used a power law relationship of amplitude to wave number k [*Mandelbrot*, 1983] with fractal dimension 2.5, following the "spectral synthesis" method of *Peitgen and Saupe* [1988]. A fractal dimension of 2.5 is compatible with values obtained for actual topography [*Turcotte*, 1997]. Surface and subsurface loads were then standardized (unit variance), and their amplitudes were scaled such that the loading ratio

$$(f) = \frac{\mathcal{W}_i(k)(\rho_m - \rho_c)}{\mathcal{H}_i(k)\rho_c} \tag{8}$$

has expected value $\mathcal{E}(f) = 1$ (although, in practice, f varies as a function of $\mathbf{k}$). Here, ρ_c and ρ_m are the densities of crust and mantle, respectively. The resulting synthetic load fields have colored noise properties similar to those expected for topographic surfaces.

[19] Vertical stresses $\rho_c g H_i$ and $(\rho_m - \rho_c) g W_i$, where g is gravitational acceleration, were applied as loads at the surface and Moho, respectively, of a thin elastic plate with a specified elastic thickness T_e. In the case of uniform T_e we calculated amplitudes of topography, $H = H_t + H_b$, and Moho deflection, $W = W_t + W_b$, from the load response relations given in Appendix A. For the case in which we examine spatially varying T_e we transformed the loads to the spatial domain and solved the fourth-order flexural governing equation using a finite difference solution [*Wyer*, 2003; *Stewart*, 1998]. For simplicity, the elastic plate was assumed to consist of a single layered crust of density ρ_c and thickness z_c overlying a mantle of density ρ_m, and subsurface loads were emplaced at the Moho. The Bouguer anomaly B was calculated from the total Moho deflection using the *Parker* [1972] finite amplitude formulation up to a fourth-order approximation. The free-air anomaly F was calculated using the first-order approximation:

$$F = B + 2\pi\rho_c GH, \tag{9}$$

where G is the gravitational constant.

[20] In the case of uniform T_e, topography and gravity were calculated on 4096 × 4096 km grids with an 8 km sampling interval. The Fourier domain calculations impose periodic boundary conditions on the spatial domain data. In order to simulate realistic data a 2048 × 2048 km nonperiodic grid was stripped from the original grid for use in the analysis of T_e recovery. We generated 100 topography-Bouguer/free-air gravity data sets for each of the uniform T_e cases examined (20, 40, 60, and 80 km). In the case of variable T_e, a 4096 × 4096 km grid would have required more computational memory than we had available. Consequently, the 2048 × 2048 km grid used to analyze the T_e recovery for the spatially varying case retains its original periodic boundary conditions. Comparisons of analyses using periodic and nonperiodic data sets with uniform T_e indicate that the bias and variance of T_e estimates are reduced when the synthetic data are periodic.

3.2. Results From Tests With Synthetic Data

[21] The synthetic data with spatially varying T_e used a structure consisting of a relatively strong (T_e = 50 km) circular region at the center, decreasing radially outward to the edges of the grid. We analyzed the coherence and admittance and tested the recovery of T_e in smaller windows centered within the larger 2048 × 2048 master grid, for window sizes of 800 × 800 km, 1000 × 1000 km, and 1200 × 1200 km. For the uniform T_e cases, bias error in T_e estimates is assessed from the difference between the true (i.e., input) T_e and the mean of the 100 T_e estimates (subsequently, we will refer to the mean estimate as the apparent or output T_e). The standard deviation in the figures is the square root of the variance. For the spatially varying T_e case we examined the mapped results of a single synthetic.

3.2.1. T_e Estimates From Theoretical Curves

[22] We first compare the observed admittance/coherence functions calculated using the multitaper method to theoretical admittance/coherence curves calculated after fixing an a priori load ratio. This has been the traditional free-air admittance approach to estimating T_e [e.g., *McKenzie*, 2003]. In light of the current controversy surrounding T_e estimation it is important to understand the difference between this approach, which yields $T_e < 25$ km in continents [*McKenzie*, 2003], and the Bouguer coherence approach proposed by *Forsyth* [1985], which yields T_e estimates from ~5 to >100 km [e.g., *Bechtel et al.*, 1987, 1989; *Lowry and Smith*, 1994]. As discussed in section 2, the *Forsyth* [1985] approach to minimizing correlation of the estimated loads has been extended in this paper to the free-air admittance function as well.

[23] In *McKenzie*'s [2003] approach, theoretical admittance functions are calculated by assuming a fixed ratio f of subsurface to surface loading that is constant for all wave numbers $\mathbf{k}$. The load ratio and T_e of the theoretical admittance are varied to find a combination of these two parameters which optimizes the fit to the observed multitaper estimate of admittance. Figure 1 shows theoretical coherence and admittance functions calculated for load ratio $f = 1$ and for T_e = 20 and 80 km. The functions were calculated assuming that subsurface loads are emplaced and compensated at the Moho, via

$$\gamma^2_{\text{theo}}(k) = \frac{\left(\frac{1}{\xi} + f^2\beta^2\phi^2\right)^2}{\left(1 + f^2\beta^2\right)\left(\frac{1}{\xi^2} + f^2\beta^2\phi^2\right)} \tag{10}$$

$$Z_{\text{theo}}(k) = 2\pi G\rho_c\left(1 - e^{-kz_c}\frac{\frac{1}{\xi} + \phi f^2\beta^2}{1 + f^2\beta^2}\right), \tag{11}$$

where

$$\xi = 1 + \frac{Dk^4}{(\rho_m - \rho_c)g}, \tag{12}$$

$$\phi = 1 + \frac{Dk^4}{\rho_c g}, \tag{13}$$

$$\beta = \frac{\rho_c}{\xi(\rho_m - \rho_c)}. \tag{14}$$

[24] Also shown in Figure 1 are multitaper estimates of the observed coherence and admittance from synthetic topography and gravity anomaly data generated with constant T_e = 20 and 80 km and subsurface loading at the Moho and expected load ratio $\mathcal{E}\{f\}$ = 1. The observed coherence and admittance curves were calculated using equations (2) and (3) for window sizes of 2000 × 2000 km, 1200 × 1200 km, and 800 × 800 km. The estimated curves are displaced toward shorter wavelengths than the corresponding theoretical curves, which were calculated from equations (10) and (11). For T_e = 80 km the rollover of the theoretical function is around 775 km, whereas the rollover of the observed coherence estimated for an 800 × 800 km window is around 400 km. This apparent bias of the estimated functions increases with decreasing window size and increasing T_e and is an artifact of the spectral estimation (which in this instance is identical to the power spectral estimation approach used by *McKenzie* [2003]).

[25] Bias in spectral estimates of the admittance and coherence is expected [e.g., *Walden*, 1990; *Simons et al.*, 2000] and can arise from any or all of several contributions. Part of the bias is inherent to the multitaper spectral estimator. Tapers are applied to the data in the spatial domain, and consequently, the estimated power spectrum is a wave number–domain convolution of the true power spectrum with the power spectral density of the tapering window. Therefore the spectral estimate at any given wave number k will include information from neighboring wave numbers ranging from $k - W$ to $k + W$, where W is the half bandwidth of the spectral estimator. When the number of tapers used is $k = 2NW - 1$, as in the case of the coherence estimate shown here, the half bandwidth is $W = 3/N\Delta$, where N is the number of samples and Δ is the sampling interval [*Walden et al.*, 1995]. As the number of tapers decreases, W decreases slightly [*Walden et al.*, 1995]. At wave numbers k near the rollover where coherence changes rapidly, the estimated coherence $\hat{\gamma}^2(k)$ will be larger than the true coherence because of leakage from spectra at $k - W$. Similarly, the estimated admittance $\hat{Z}(k)$ will be smaller than the true admittance because of leakage from spectra at $k - W$. These effects are amplified by the fractal dimensions of the signals, which favor larger amplitudes (and, hence, more significant leakage) from the $k - W$ side of the wave band than from the $k + W$ side. For a fixed NW, as used here, as the window size decreases (N decreases), W increases and the bias of the coherence/admittance estimate toward the true value at longer wavelengths increases. Averaging of the spectra within wave number bins in equations (3)–(5) can further bias the estimates of coherence and admittance because the larger amplitudes at smaller wave numbers will dominate the calculation.

[26] When the observed and predicted admittance and coherence are calculated using the same multitaper power spectral estimator for each, as is done for the coherence method and for the revised admittance method described in section 3, then the bias of the observed and predicted functions should be approximately the same. Similar biases would cancel in equations (6) and (7) and so would not result in significant bias of the T_e estimate. However, if the observed multitaper admittance is compared to a theoretical admittance such as is described in equation (11) [e.g., *McKenzie*, 2003], the T_e estimates will be biased toward lower values. The bias in the estimate of T_e depends on the size of the estimation window, the true T_e, and the multitaper windowing scheme. For the multitaper parameters used here (NW = 3) and a 2000 × 2000 km analysis window, the best fit T_e from applying equation (7) to difference the estimated admittance with equation (11) is ~35 km for synthetic data generated with a true T_e = 80 km. Therefore we expect that T_e estimates obtained by comparing observed multitaper estimates of coherence or admittance to theoretical curves [e.g., *McKenzie*, 2003] will be biased toward much lower values unless the analysis windows are extremely large, i.e., $\gg$2000 × 2000 km. However, analysis windows of this size are likely to yield an average of the true spatially varying T_e. To recover spatial variations in T_e, methods such as those used here or those based on wavelet analysis should be used [e.g., *Stark et al.*, 2003; *Simons et al.*, 2003].

[27] It is also worth noting that when T_e is large, the maximum observed coherence decreases as window size decreases in Figure 1. Conversely, the minimum observed admittance increases as window size decreases. This reflects undersampling of the long wavelengths where the diagnostic rollover occurs. Hence low coherence at the longest wavelengths does not necessarily indicate a geological effect such as erosion and sedimentation, and large admittance at these wavelengths need not indicate dynamic support of the topography, as has been inferred, e.g., by *McKenzie* [2003]. However, high admittance and low coherence at the longest wavelengths of the spectral estimates can degrade the recovery of T_e using the methods described here. We have attenuated this degradation by neglecting the first three admittance/coherence values at the longest wavelengths in the calculation of the misfit error between observed and predicted coherence/admittance.

[28] A final effect that is worth noting is that the multitapered coherence curves (observed and predicted) do not go to zero at short wavelengths. This is probably due to the bias intrinsic in the estimation of the spectra. As the number of tapers used increases, the variance of the spectra is reduced and the coherence at short wavelengths becomes closer to zero [see *Simons et al.*, 2000, Figure 5].

3.2.2. Estimates of Uniform T_e

[29] Figure 2 shows histograms of T_e recovered from synthetic data sets with true T_e = 20, 40, and 80 km and a load ratio f = 1. Each of the histograms shows the result of admittance or coherence analysis for 100 sets of synthetic topography, Bouguer, and free-air gravity data. As noted in section 3.1, the surface and subsurface loads were deconvolved within 2048 × 2048 km windows, and in Figure 2 a window of 1000 × 1000 km centered within the deconvolution window was used to calculate the predicted admittance and coherence functions.

[30] For both the coherence and admittance approaches the bias and variance of the T_e estimate increase with increasing true T_e, as observed previously for the Bouguer coherence approach [*Macario et al.*, 1995; *Ojeda and Whitman*, 2002; *Swain and Kirby*, 2003a]. Also the number of outlier estimates increases as T_e increases. We define outliers as T_e estimates >130 km. In such cases the misfit curve between observed and predicted coherence or admittance is flat at high T_e values, and the best fit T_e is effectively unconstrained.

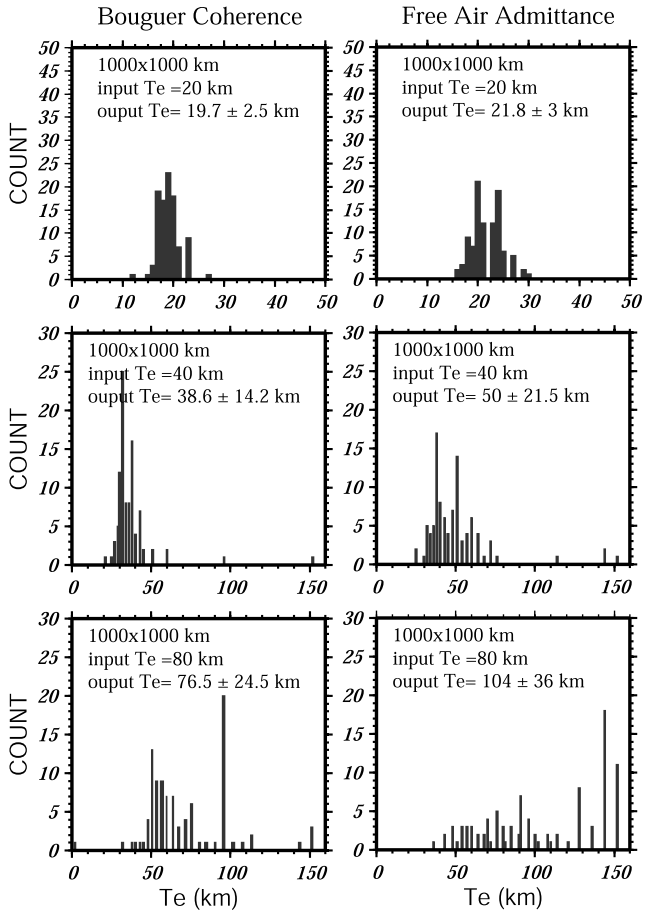

Figure 2. (left) Histograms of 100 Bouguer coherence and (right) free-air admittance analyses of synthetic data generated with input or "true" T_e = 20, 40, and 80 km and an average loading ratio of $f = 1$. The window size used for analysis was 1000 × 1000 km. Output T_e is the mean and standard deviation resulting from the 100 analyses.

[31] Our analyses of T_e recovery use data that are nonperiodic within the deconvolution window, and hence our results are not directly comparable to previous studies where periodic data were used [*Macario et al.*, 1995; *Swain and Kirby*, 2003a; *Ojeda and Whitman*, 2002]. We chose to use nonperiodic data because real data are also nonperiodic. Comparison to tests performed with periodic data indicates that nonperiodic synthetics result in T_e estimates with greater variance and more outliers, indicating that nonperiodicity degrades the recovery of T_e.

[32] In Figure 3 we construct error curves of true T_e versus estimated T_e similar to those of *Swain and Kirby* [2003a]. Each of the plots of apparent T_e represents the mean of 100 tests with true T_e = 20, 40, 60, or 80 km. We repeat these tests for window sizes of 800 × 800 km, 1000 × 1000 km, and 1200 × 1200 km. We also plot the standard deviation of the estimates in each of the cases. For both coherence and admittance the bias and standard deviation increase with increasing true T_e and with decreasing window size. When all of the estimates are included in the mean, the bias using Bouguer coherence is very small (Figure 3a). However, when outlier estimates of T_e > 130 km are not included in the means, the estimated T_e is biased slightly downward (Figure 3c), as noted previously by *Ojeda and Whitman* [2002] and *Swain and Kirby* [2003a], and the standard deviation is significantly reduced

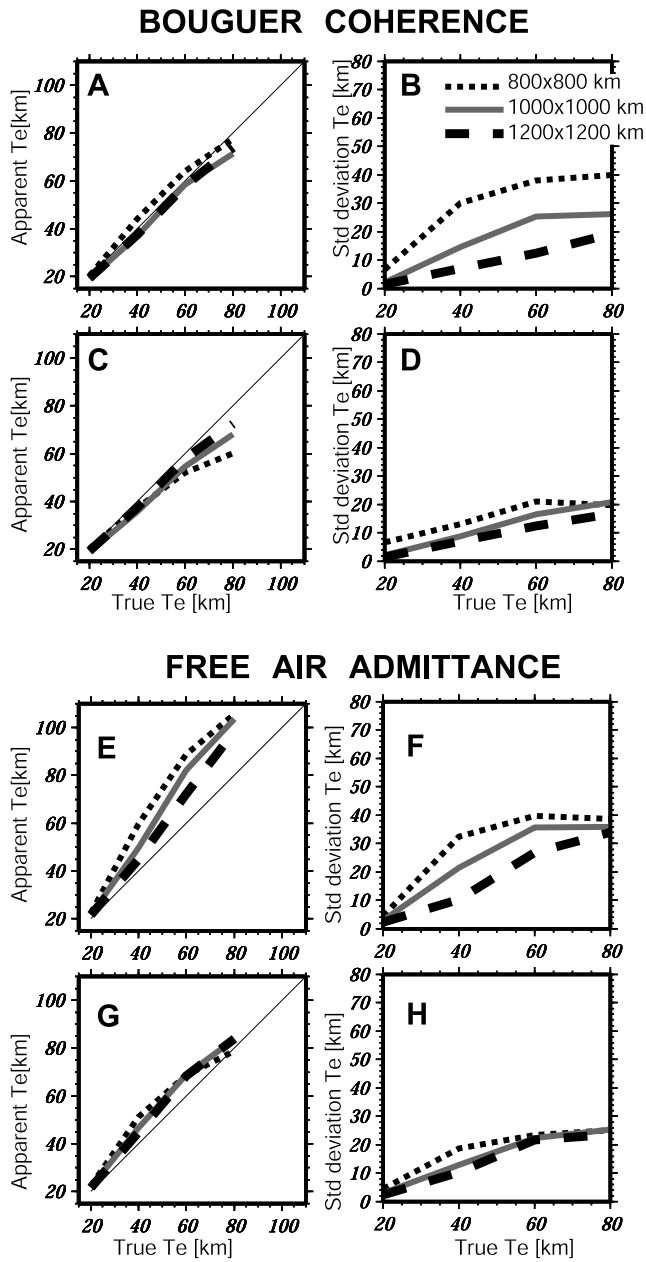

Figure 3. (a) Mean or apparent T_e resulting from 100 Bouguer coherence analysis using synthetic data generated with input T_e of 20, 40, 60, and 80 km and an average loading ratio $f = 1$. Results using 800 × 800, 1000 × 1000, and 1200 × 1200 km analysis windows are shown (see legend). (b) Standard deviation of the 100 Bouguer coherence results whose mean is shown in Figure 3a. (c, d) The same as in Figures 3a and 3b, respectively, but only considering T_e estimates which are smaller or equal than 130 km. (e, f) the same as in Figures 3a and 3b but using the free-air admittance function to estimate T_e. (g, h) the same as in Figures 3e and 3f but only considering T_e estimates which are smaller or equal than 130 km.

(Figure 3d). The bias in T_e estimates increases with decreasing window size, correlative with an increase in the number of outliers. Figures 2 and 3 also demonstrate that the Bouguer coherence approach recovers T_e slightly more accurately than the free-air admittance method (Figures 3e–3f). *Banks et al.* [2001] also note this and suggest that it is because the free-air gravity anomaly is more perturbed by leakage effects because of the relatively low power of the free-air gravity anomaly at long wavelengths.

[33] Although bias error can be significant when small windows are used to estimate a large T_e, the variance of T_e estimates poses a greater problem. Note, for example, in Figure 3 that for an input T_e = 60 km the bias error using Bouguer coherence is similar for 800 × 800 and 1200 × 1200 km windows but the standard deviation for the smaller window is 3 times larger. Hence a careful study of T_e variations within a region should include multiple analyses using various window sizes to avoid interpreting random errors as true variations in lithospheric strength.

3.2.3. Estimates of Spatially Varying T_e Structure

[34] Both the coherence and admittance methods assessed in this paper assume that T_e is constant throughout the analysis region. However, in reality, T_e is expected to vary between different geologic terrains. To test the recovery of spatially varying T_e, we generated synthetic data with a known variable T_e structure consisting of a strong circular core with diameter of ~600 km and T_e = 50 km, surrounded by lithosphere that weakens radially outward from the center of the region (Figure 4d). The T_e analysis used constant-sized, overlapping windows with centers spaced 56 km apart. The entire data set was 2048 × 2048 km with an 8 km sampling interval and loading ratio f = 1. Figure 4 shows T_e estimates using the Bouguer coherence analysis within 1200 × 1200, 1000 × 1000, 800 × 800, and 600 × 600 km windows (Figures 4e–4h) and the free-air admittance analysis within 1200 × 1200, 1000 × 1000, and 800 × 800 windows (Figures 4a–4c).

[35] The Bouguer coherence estimates bear little resemblance to the true T_e structure when estimation windows are small (Figure 4h), with T_e varying significantly on short spatial scales and departing significantly from the true value. This result is consistent with the uniform T_e tests in which the variance of T_e estimates was high for large T_e (>40 km) and small window size. The very high T_e values at the center of the region are outliers similar to those observed for uniform T_e. As window size increases, the estimates stabilize. Using 800 × 800 km estimation windows (Figure 4g), the spatial distribution of T_e is more similar to the true T_e, although the circular area with highest T_e values is smaller. When the size of the estimation window increases further, the estimates are smoothed and T_e estimates at the center of the region are biased even further downward (Figures 4f and 4e). In Figures 4i–4l the estimates of maximum coherence are shown for all window sizes. As observed for uniform T_e synthetics (see Figure 1), maximum coherence decreases with decreasing window size.

[36] In the case of the free-air admittance method (Figures 4a–4c) the dependence of T_e estimates on window size exhibits similar properties to those of the Bouguer coherence. However, the T_e estimates tend to be more biased upward than in the coherence case, as observed earlier for estimates of uniform T_e (Figure 3).

[37] In contrast to the results obtained with a uniform T_e structure, when T_e is spatially variable, there is a trade-off between spatial resolution and variance. Trade-offs between variance and resolution bias are common in geophysical inverse problems [e.g., *Menke*, 1989]. T_e estimation windows that are too small introduce spurious spatial variations, whereas very large windows can make the estimates appear smoother than the true structure. In the limiting case in which the T_e estimation window is 2048 × 2048 km (i.e., the size of the synthetic data grid), Bouguer coherence and free-air admittance analysis yield a T_e estimate of 21.4 and 32 km, respectively, which is close to half of the highest (50 km) and lowest (0 km at the edges) T_e values but higher than the average T_e which is 13.3 km.

3.3. Summary

[38] In section 3 we have tested the recovery of T_e using the Bouguer coherence and free-air admittance methods with a multitaper filtering technique. We find that comparison of observed multitapered admittance/coherence functions to theoretical admittance/coherence functions leads to underestimation of the underlying T_e. When observed multitapered admittance/coherence functions are compared to predicted multitapered admittance/coherence functions, we find the following:

[39] 1. The bias and variance in Bouguer coherence and free-air admittance estimates increase for larger true T_e and for smaller windows. Bouguer coherence estimates tend to be biased slightly downward, while free-air admittance estimates are biased upward.

[40] 2. The Bouguer coherence method yields estimates with lower variance relative to the free-air admittance, for a given estimation window size. This is related to greater sensitivity to leakage due to high power in the short wavelengths and low power in the long wavelengths of the free-air gravity spectra.

[41] 3. T_e estimation using sliding, overlapping windows can recover a T_e structure which well approximates the spatial variability, but the window size must be chosen carefully to minimize both the variance and smoothing bias. Windows that are too small introduce spurious spatial variations, and windows that are too large tend to average the spatially varying T_e values and smooth the true structure. Because free-air admittance estimates have larger variance than those using Bouguer coherence, the optimal window size for the admittance method is larger (and hence lower resolution) than for the coherence method.

4. Part 2: T_e Structure of Fennoscandia From Spectral Analysis

4.1. Tectonic Setting

[42] The lithospheric structure of Fennoscandia results from several Archean to Paleozoic orogenies. Fennoscandian lithosphere has three principal domains (Figure 5): the Archean domain in the east, the Svecofennian domain in the central region, and the Scandinavian domain in the southwest [*Gaal and Gorbatschev*, 1987].

[43] The Archean domain was formed during the Samian (3.1–2.9 Ga) and Lopian (2.8–2.6 Ga) orogenies. The Karelian province is the core of the Archean domain. Although the crust in the region has remained relatively

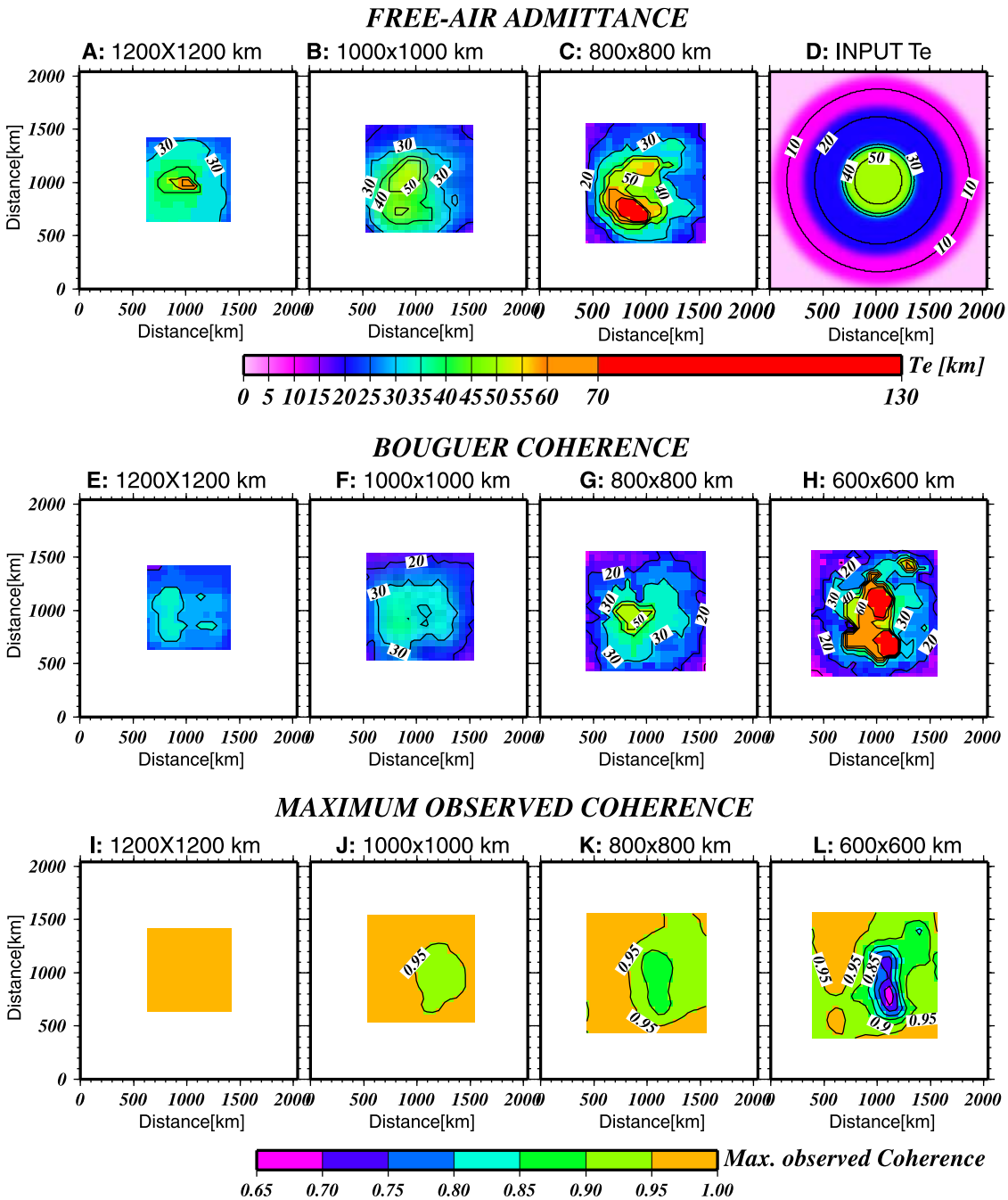

Figure 4. T_e estimates of the spatially varying T_e structure shown in Figure 4d (input T_e). Estimates using free-air admittance with analysis windows of (a) 1200 × 1200 km, (b) 1000 × 1000 km, and (c) 800 × 800 km. Estimates using Bouguer coherence with analysis windows of (e) 1200 × 1200 km, (f) 1000 × 1000 km, and (g) 800 × 800 km and (h) 600 × 600 km. (i–l) Maximum observed coherence for each of the analysis windows used in Figures 4e–4h.

undeformed since Archean times, it experienced several Paleoproterozoic extensional events between ~2.5 and 2.0 Ga. Compilations of seismic refraction profiles by *Korsman et al.* [1999, and references therein] indicate that the average crustal thickness in the region is 42 km (Figure 6). A high-velocity (>7 km/s) lower crustal layer up to 8 km thick has been interpreted as mafic underplate resulting from Paleoproterozoic extensional episodes. The Lapland-Kola orogen flanks the Karelian province to the north and was probably formed by the collision of several Archean crustal blocks at ~2.0 to 1.9 Ga [*Korsman et al.*, 1999, and references therein]. Later reworking and deformation of the Kola peninsula is manifest in the formation of the White Sea rift and the development of Neoproterozoic rift basins beneath the present-day Barents Sea [*Korsman et al.*, 1999]. The average thickness of the crust there is 43 km (Figure 6).

[44] The Paleoproterozoic Svecofennian domain is thought to have formed by collision between the Archean Karelian craton and a Paleoproterozoic island arc between 1.9 and

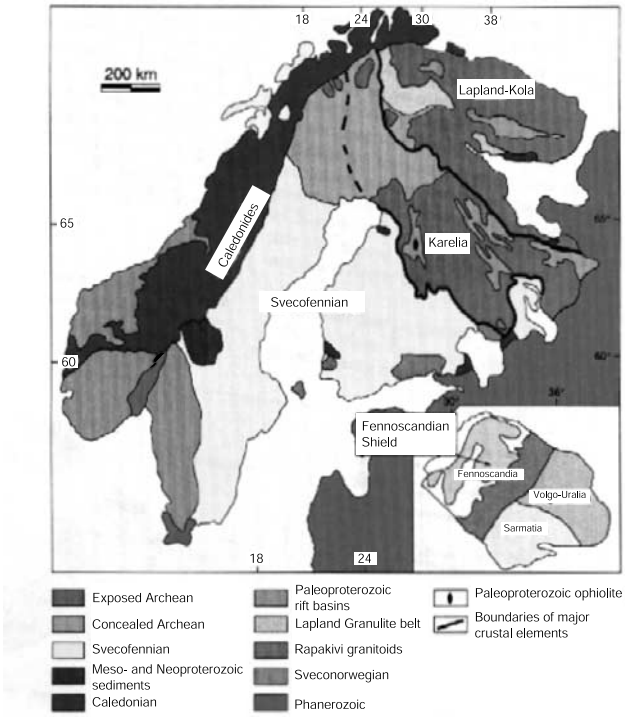

Figure 5. Simplified tectonic map of Fennoscandia [after *Hjelt and Daly*, 1991]. Svecofennian domain is Proterozoic in age and the Caledonian and Sveconorwegian are Phanerozoic.

1.55 Ga [*Windley*, 1993]. This orogeny produced some of the thickest continental crust anywhere on Earth, excluding active orogenies, at >55 km [*Korsman et al.*, 1999] (Figure 6). Most of the Moho depth variations can be explained by variations in thickness of a high-velocity (V_p > 7 km/s), high-density (>3000 kg m^{-3}) lower crustal layer [*Korsman et al.*, 1999] (Figure 6). In Finland the crust varies from ~40 km at the southern coast to ~60 km in the center. The lower crustal layer is on average 21 km thick and is thought to represent magmatic underplate [*Korsman et al.*, 1999]. Topography in this domain is subdued with ~100–200 m of total relief, and the Bouguer anomaly exhibits little correlation with crustal thickness (Figures 6 and 7), possibly indicating that the density contrast at the Moho is small.

[45] The youngest part of the Fennoscandian Shield, the Scandinavian domain, was probably formed during the Gothian event (1.75–1.5 Ga). After this event the crust was reworked during the Sveconorwegian-Grenvillian (1.25–0.9 Ga) and Caledonian (0.6–0.4 Ga) orogenies [*Gaal and Gorbatschev*, 1987]. The Oslo graben opened as an intracontinental rift during the last tectonically active phase between 305 and 245 Ma, and most recently, the west coast of Norway was thinned and uplifted during the opening of the North Atlantic in Cretaceous-Tertiary time.

4.2. Lithospheric Structure

[46] Early studies of Rayleigh wave dispersion data indicated that the thickness of the high-velocity seismic lid varies from 110 km under the coast of Norway, southern Norway, and Sweden and increases toward the Gulf of Bothnia and central Finland, reaching a thickness of more than 170 km [*Calcagnile*, 1982]. More recently, analysis of high-resolution body wave tomography in central Finland indicates that the seismic lid extends at least to 300 km depth [*Sandoval et al.*, 2003]. If lid thickness is related to the mantle geotherm, we expect that variations in seismic lid thickness will correlate with variations of T_e [*Watts et al.*, 1980; *Watts and Zhong*, 2000].

4.3. Previous Studies

[47] The earliest estimates of elastic thickness of Fennoscandia were based on modeling observations of postglacial rebound. In models of postglacial rebound a viscoelastic mantle is overlain by an elastic layer. The thickness of this uppermost elastic layer is not directly equivalent to T_e as defined here because of the dependence of effective elastic thickness on the timescale of loading [e.g., *Willett et al.*, 1984, 1985] and because part of the stress integrated into the effective elastic thickness in spectral gravity/topography studies resides in the ductile flow regime, which is modeled as viscoelastic in rebound studies. Nevertheless, the elastic thickness, or at least its relative variations, obtained from postglacial rebound should be closely related to the T_e that we will estimate here. *Wolf* [1987] suggests a flexural rigidity less than 5×10^{24} N m (T_e = 80 km for Young's modulus $E = 10^{11}$ Pa) based on observations of sea level changes from central Sweden and Finland. *Lambeck et al.* [1990] estimate a range of T_e values of 100–150 km from inversion of sea level observations. *Mitrovica and Peltier*

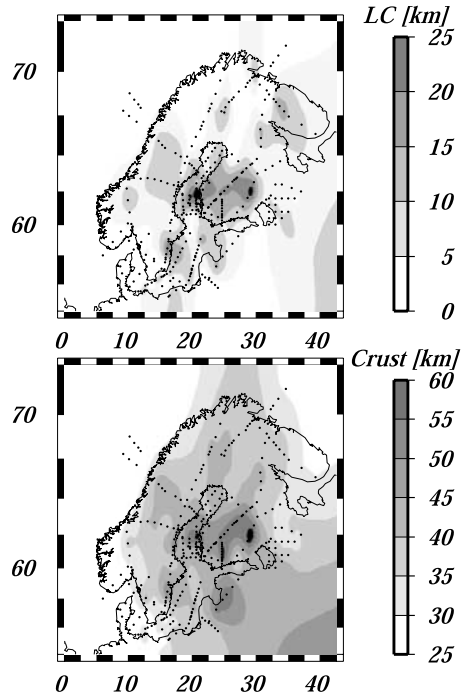

Figure 6. (top) Thickness of the lower crustal layer with velocities more than 7 km/s. (bottom) Crustal thickness in Fennoscandia. Dots are data points obtained form seismic refraction used for interpolation (data compiled by *Korsman et al.* [1999]).

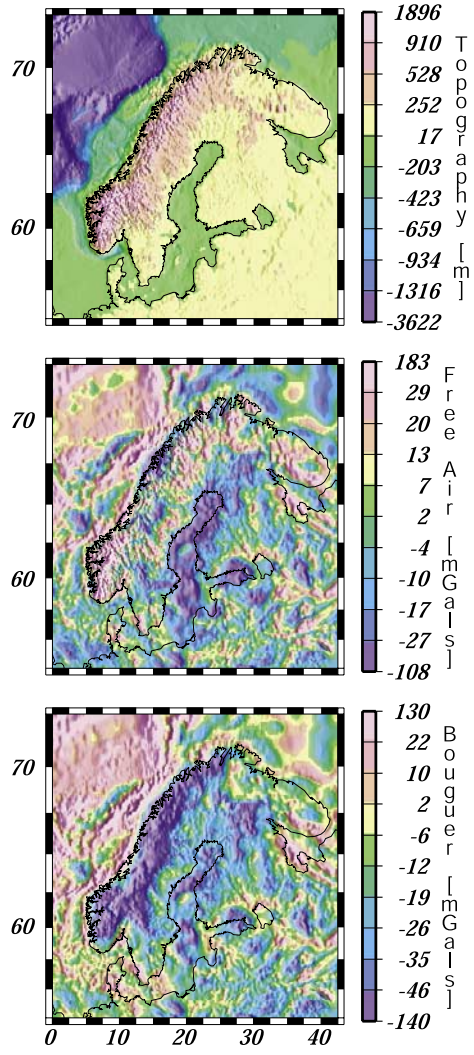

Figure 7. Topography, free-air, and Bouguer gravity anomaly used in this study.

[1993] suggest T_e ranging from 70 to 145 km ($E = 10^{11}$ Pa) from Fennoscandian uplift data. None of these studies consider the possibility of laterally varying T_e. However, *Fjeldskaar* [1997] examined T_e variations using the present rate of uplift as well as tilts of paleoshorelines at the former ice sheet margin. The elastic thickness varies from 20 km ($E = 10^{11}$ Pa) at the Norwegian coast to more than 50 km in central parts of Fennoscandia for his most likely ice model. Comparing GPS observations with numerical predictions, *Milne et al.* [2001] estimated an elastic thickness for Fennoscandia of 90–170 km.

[48] In addition to the rebound studies, *Poudjom Djomani et al.* [1999] use Bouguer coherence of gravity and topography with a periodogram spectral estimator to estimate T_e in Fennoscandia. They used analysis windows which are irregularly sized and spaced and thus are not expected to have uniform resolution or errors. Also, these windows do not cover Fennoscandia evenly. The Caledonides and southern Norway and Sweden are well sampled with small overlapping analysis windows, but in the Karelian domain and the Finnish Svecoffenides, there are only two large analysis windows. The Kola peninsula is also poorly sampled by only two T_e estimates. They obtain T_e values of <12–20 km for the Caledonides, around 20–28 km for the Swedish Svecofennian and the Sveconorwegian domains, 40–68 km for the Karelian province, and 48–60 km for the Kola peninsula (using $E = 10^{11}$ Pa). On the basis of these results they infer a positive correlation between T_e, the age of the last tectonothermal event and the lithospheric mantle composition.

[49] The purpose of section 4.4 is to carry out a more detailed study of T_e which covers all regions of Fennoscandia using overlapping analysis windows. As discussed in section 2, we use a multitaper spectral estimator which yields more accurate representations of the power spectra than the mirrored periodogram technique used by *Poudjom Djomani et al.* [1999]. We examine six different estimates of mapped T_e for Fennoscandia, obtained using three different analysis window sizes and both the Bouguer coherence and free-air admittance functions. In light of the synthetic data analysis in section 3, we assess the validity of the results with careful attention to window size issues. We also compare the T_e structure obtained using the Bouguer coherence and free-air admittance techniques.

4.4. Topography and Gravity Anomaly Data

[50] The topography and gravity anomaly data used in this study (Figure 7) were compiled by GETECH (UK) as part of their West Europe Gravity project. The elevation data consist of topographic and bathymetric data from land surveys and ship track data. The gravity data, free-air offshore and Bouguer onshore, were acquired through land and marine surveys and satellite-derived free-air gravity where the ship track density was low. Terrain corrections were applied to the onshore Bouguer gravity data. The grid interval is 8 km, and data are projected in a Lambert conformal conic projection.

[51] The Bouguer coherence analysis was performed after converting the offshore free-air gravity data, F_{off} to Bouguer anomaly, B_{off} using the slab formula and a surface rock/water density contrast of $\Delta\rho = 1670$ kg m^{-3}, applied to the bathymetry data:

$$B_{\text{off}} = F_{\text{off}} + 2\pi\Delta\rho GH. \tag{15}$$

Conversely, for the free-air admittance analysis, onshore Bouguer anomaly data B_{on} were converted to free-air anomaly F_{on} by again using the slab formula and a density contrast between surface rock and air of $\rho_0 = 2670$ kg m^{-3} (Figure 7):

$$F_{\text{on}} = B_{\text{on}} + 2\pi\rho_0 GH. \tag{16}$$

Appendix A explains how we estimated T_e in land and ocean areas.

5. T_e Structure

[52] To recover spatial variations of T_e in Fennoscandia, we analyzed overlapping analysis windows with centers separated at 56 km intervals. To obtain high spatial resolution and at the same time recover potentially high T_e, we used three window sizes: 800 × 800 km, 1000 × 1000 km,

and 1200 × 1200 km for the Bouguer coherence analysis and 1000 × 1000 km, 1200 × 1200 km, and 1400 × 1400 km for the admittance analysis. To simplify the discussion that follows, we will designate T_e obtained from Bouguer coherence analysis as "coherence T_e" and the T_e recovered from free-air admittance analysis as "admittance T_e." When a statement holds for both coherence and admittance estimates, we simply refer to it as "T_e."

[53] We found that T_e structure determined from coherence and admittance analysis is similar over Fennoscandia. In general, the admittance T_e tends to be larger than the coherence T_e. This result is consistent with that obtained from synthetic data, where coherence and admittance estimates tend to underestimate and overestimate, respectively, the true T_e (Figures 2, 3, and 4). The synthetic results also show that as the true T_e increases, the discrepancies between coherence and admittance estimates also increase (Figures 2 and 3). Similarly, in Fennoscandia the admittance and coherence T_e estimates differ most where T_e is high, e.g., in the Proterozoic domain of central Finland, the Archean Karelia, and the Kola peninsula (Figures 8a and 8b).

[54] Figure 8 shows that T_e estimates increase from ~20–25 km near the coasts of western and southern Norway and southern Sweden to very high values (>60 km) in Svecofennian central Finland and parts of the Karelian domain. For the smallest windows the increase in T_e in the east-west direction is more abrupt than for larger windows, where the T_e structure appears smoother. This pattern is analogous to the observation from synthetic data that larger analysis windows smooth the true structure of spatially varying T_e (Figure 4). T_e estimates for the Caledonides are relatively unchanged with increasing window size and are around 20–40 km. Estimates for the Kola peninsula are also insensitive to window size, yielding coherence T_e estimates from ~40 to 50 km and admittance T_e estimates from ~60 to 70 km.

[55] As window size increases, T_e in the Swedish Svecofennides decreases from values of 40–60 km to estimates of 30–40 km. Similarly, the coherence T_e in the Gulf of Bothnia decreases from values of 70–90 km for the smallest windows to values of 40–60 km for the largest windows. In the same region the admittance T_e decreases from values of 70–130 km for the smallest windows to values of 50–80 km for the larger windows.

[56] In central Finland and the southern Karelian domain, coherence T_e varies irregularly and attains very high values of 80–110 km when the smallest window is used (Figure 8b; note that T_e estimates >130 km are not shown). As the window size increases, the variations in coherence T_e become smoother, and T_e stabilizes to values of 70–100 km. Judging from the T_e recovery in synthetic tests (Figure 4), an 800 × 800 km window is probably too small to recover T_e in Archean regions of Fennoscandia, and the 70–100 km estimate from 1200 × 1200 km windows is probably more accurate. Figure 8c illustrates how the maximum observed coherence at every analysis location decreases with decreasing size of the analysis window. For an 800 × 800 km window the maximum coherence is <0.2 over some areas, indicating that T_e estimates from such a small window are unlikely to be reliable. Figure 9 illustrates in more detail why coherence T_e estimates depend so strongly on window size. Figure 9 shows the observed and best fit predicted coherence for all three window sizes, together with the corresponding misfit, for locations in the Caledonides and in central Finland. T_e at the site in the Caledonides is around 33 km and does not vary significantly with window size, changing by only ±2 km when the window size is changed (Figure 9a). In central Finland, however, maximum coherence is very small for the smallest window and increases for larger windows (Figure 9b).

[57] The admittance T_e in central Finland is very high, with estimates ranging from 115 to 130 km for the smallest window size (Figure 8a). Admittance T_e in this region decreases to 70–130 km for the largest windows. Figures 10a and 10b show typical observed admittance functions from the Caledonides and from central Finland. As observed previously for the coherence estimate, the admittance T_e from the Caledonides varies only slightly with window size, while in central Finland it varies considerably. The smallest window size in this location yields very high estimates of admittance at long wavelengths, exhibiting a peak at around 200 km wavelength and then decreasing for smaller wavelengths (Figure 10b). The T_e estimate from this admittance function is 128 km. As the window size increases, both the admittance at long wavelengths and the peak at 200 km wavelength decrease. The best fit T_e decreases as well. For the largest window used in this study (1400 × 1400 km) the peak has nearly disappeared, and the admittance nears zero at the longest wavelengths. Figure 10c shows the observed admittance from synthetic data with $f = 1$ and uniform $T_e = 80$ km. Figure 10c illustrates similar features to those observed in the real data: the admittance is relatively high at long wavelengths and a peak is observed near 200 km wavelengths when the smallest window is used. As the window size increases, the admittance and the peak decrease. This is accompanied by a decrease in the best fit T_e, which is closest to the true T_e when the window size is largest. We expect that the admittance T_e recovered using the smallest windows overestimates the true T_e, so the 70–120 km estimates recovered with the largest window are likely to be the most accurate. These are slightly larger than the coherence T_e estimates, and we conclude that T_e of the Proterozoic lithosphere in central Finland is in the 70–100 km range.

6. Discussion

[58] We have obtained a detailed T_e map of Fennoscandia using Bouguer coherence and free-air admittance analyses of overlapping windows. We have shown that the two types of analyses give similar estimates, so long as both methods explicitly calculate the location- and wavelength-dependent surface and subsurface loading using the method of *Forsyth* [1985]. Both methods yield T_e of 20–40 km in the Caledonides, 40–60 km in the Swedish Svecofennides, 40–60 km in the Kola peninsula, and 70–100 km in the southern Karelia province and Svecofennian central Finland.

[59] Given that the maximum crustal thickness in Finland is around 60 km, these results support the expectation based on laboratory analyses of rock rheology that the mantle contributes a significant fraction of total lithospheric strength in old, cold, stable continental regions. Recently, a group of researchers has challenged this viewpoint, arguing that T_e estimates obtained from stable cratonic lithosphere using Bouguer coherence are overestimates of

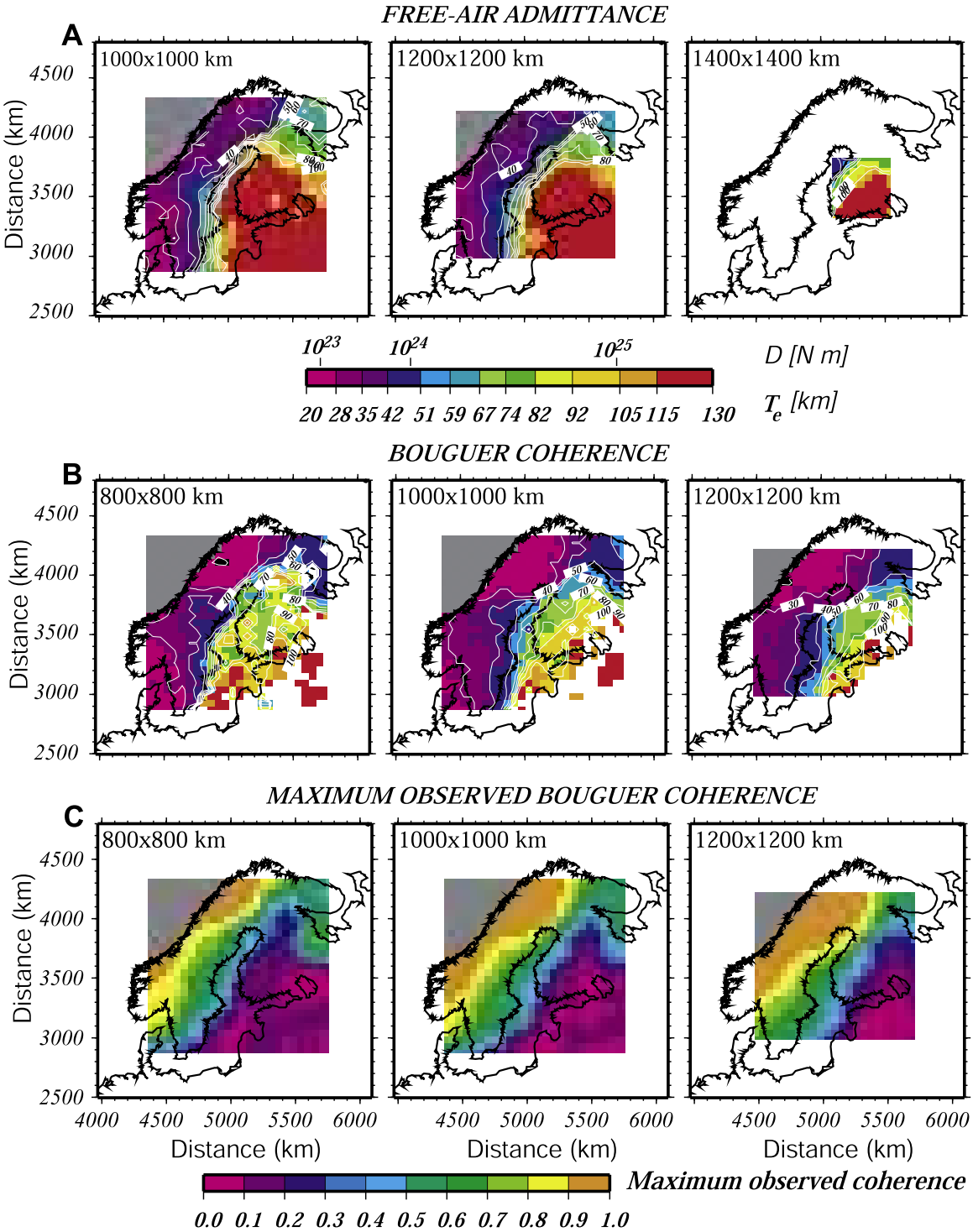

Figure 8. T_e estimates of Fennoscandia using (a) free-air admittance and (b) Bouguer coherence. Window sizes are indicated. T_e results >130 km are not shown. (c) Maximum observed coherence in each of the windows analyzed in Figure 8b.

the true T_e [*McKenzie and Fairhead*, 1997; *Maggi et al.*, 2000; *Jackson*, 2002; *McKenzie*, 2003]. *McKenzie* [2003], in particular, argues that erosion and sedimentation tend to flatten the topography, and thus reduce the response of the crust to subsurface loading. This is, of course, inconsistent with a thin plate approximation of flexural isostasy, for which the removal of compensating topography would require readjustment until the load was completely compensated by internal flexural deflections. However, a combination of thick plate stress effects and depth-dependent gravity response could result in gravity anomalies that are "incoherent" with the topography, as implicitly suggested by *McKenzie* [2003]. In that case, Bouguer coherence as estimated from equation (10) could overestimate T_e

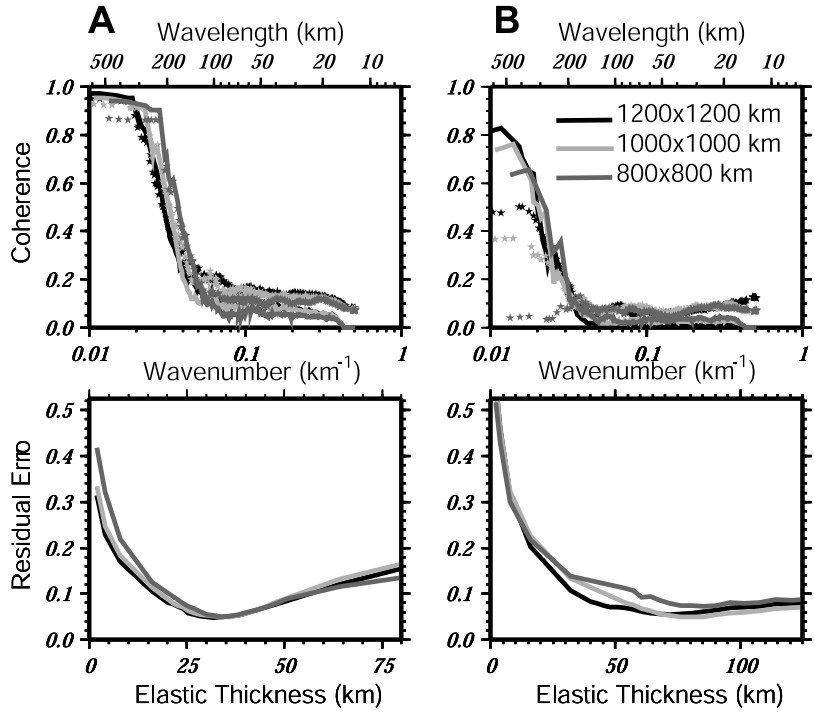

Figure 9. (a) (top) Bouguer coherence curves for a site in the Caledonides. Stars are observed coherence curves for different sizes of the analysis window. Solid lines are predicted coherence curves for each of the analysis windows. Gray tones indicate results with different analysis windows (see legend). (bottom) Corresponding error curves. Best fit T_e for 1200 × 1200 km analysis window is 32 km, for 1000 × 1000 km is 35.9 km, and 800 × 800 km is 33.9 km. (b) Same as in Figure 9a but for a site in central Finland. In this case, the best fit T_e is 71.8 km for 1200 × 1200 km analysis window, 80.6 km for 1000 × 1000 km analysis window, and 85.4 km for 800 × 800 km analysis window.

[*McKenzie*, 2003]. *McKenzie* [2003] therefore recomputed T_e for various regions using free-air admittance since, in his view, only the part of the free-air gravity that is reflected in the topography can be used to estimate T_e. He found that T_e is small and of the order of the seismogenic thickness ($T_e <$ 25 km). This and similar results from earlier work have led some researchers to hypothesize that the strength of the continental lithosphere resides in the seismogenic layer in the crust and the mantle is relatively weak [*Maggi et al.*, 2000; *Jackson*, 2002].

[60] In the following sections we (1) discuss the possible effects of unmodeled noise processes which might potentially bias our T_e estimates of Fennoscandia such as postglacial rebound and the occurrence of incoherent subsurface loads, (2) use geotherms derived from mantle xenoliths and constraints on crustal composition to independently estimate the T_e expected from integration of lithospheric stress, and (3) discuss the relationship of our T_e estimates with other lithospheric parameters such as tectonic age, heat flow, and seismogenic thickness.

6.1. Effects of Unmodeled Noise in Coherence and Admittance Estimates of T_e

6.1.1. Effect of Postglacial Rebound on T_e

[61] The Bouguer coherence and free-air admittance methods, as formulated here, assume that the gravity and topography signals are a result of flexural compensation of surface and subsurface loads. These methods do not take into account possible dynamic effects. One such effect in Fennoscandia derives from incomplete isostatic adjustment following the removal of Quaternary ice loads. The unrecovered portion of the postglacial rebound (PGR) will be a source of noise in the coherence and admittance analysis if the unrecovered PGR deflections are large at the wavelengths of transitional isostatic behavior.

[62] *McConnell* [1968] measured the past uplift due to PGR from the elevation of paleoshorelines in Fennoscandia and showed that the spectrum of the past uplift has two amplitude peaks. The main and secondary peaks have wavelengths of 1800 km and ~480 km, respectively. If these peaks are also present in the unrecovered glacial deflection, the secondary peak could conceivably bias our T_e estimates. To obtain an estimate of T_e free of potential noise introduced by PGR, we used estimates of unrecovered uplift calculated from the past uplift history assuming an ice load model and mantle viscosity parameters (J. Wahr, personal communication, 2003; see Figure 11 for parameter description). The estimates of unrecovered PGR displacement used here represent a "worst case" scenario, i.e., have a bigger amplitude than those derived using other possible mantle viscosities. Thus we expect that if T_e is not biased by the unrecovered PGR displacements analyzed here, it will not be biased by unrecovered PGR displacements calculated using other mantle viscosities. Our approach is to add the model of unrecovered surface deflection to the present topography in Fennoscandia and

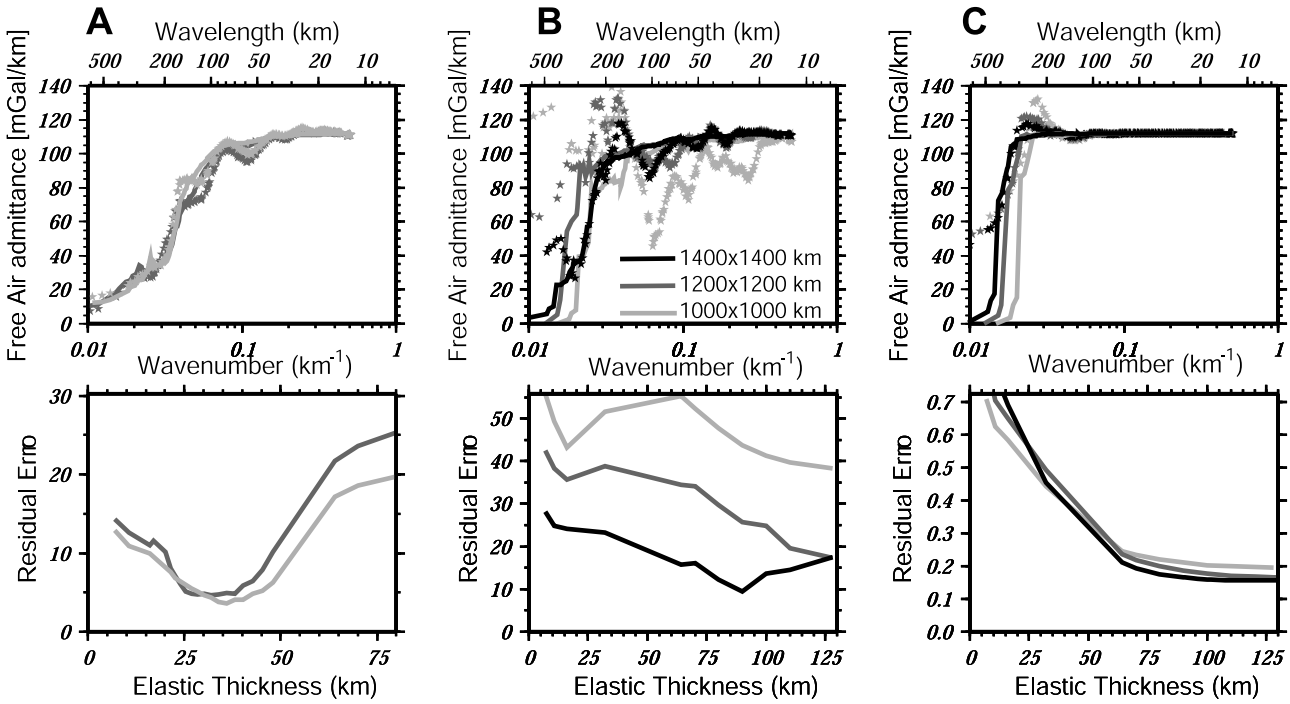

Figure 10. (a) (top) Free-air admittance curves for a site in the Caledonides. Stars are observed admittance curves for different sizes of the analysis window. Solid lines are predicted admittance curves for each of the analysis windows. Gray tones indicate results with different analysis windows (see legend). (bottom) Corresponding error curves. Best fit T_e is 32 km for 1200 × 1200 km analysis window and 35.9 km for 1000 × 1000 km analysis window. (b) Same as in Figure 10a but for a site in central Finland. In this case, the best fit T_e is 90 km for 1400 × 1400 km analysis window, 128 km for 1200 × 1200 km analysis window, and 128 km for 1000 × 1000 km analysis window. (c) Same as in Figure 10b but for synthetic data generated with a T_e = 80 km and an average loading ratio of 1. The best fit T_e is 120 km for 1400 × 1400 km analysis window, 143 km for 1200 × 1200 km analysis window, and 128 km for 1000 × 1000 km analysis window.

to compute new free-air and Bouguer anomaly fields from the revised topography. The "corrected" topography and gravity anomalies represent a hypothetical future state in which all of the surface deflection due to past glacial loading has disappeared. Using the corrected data, we calculated a new T_e structure using Bouguer coherence and free-air admittance. The results (Figure 12) are very similar to those in which the glacial loading effect was uncorrected (Figure 8) and therefore indicate that the unrecovered surface deflection does not bias the T_e estimates presented in section 7.

6.1.2. Effect of Incoherent Loads on T_e

[63] Another potential source of noise has been hypothesized by *McKenzie* [2003], who argues for the existence of internal loads without topographic expression, or "incoherent noise." The argument holds that erosion and sedimentation can reduce the landscape to a perfectly flat plane, thus removing the topographic response to internal loads. These incoherent loads would generate a Bouguer gravity signal that is uncorrelated with topography, and *McKenzie* [2003] argues that Bouguer coherence in the presence of such loads will overestimate T_e. He suggests that in locations where incoherent loading dominates, such as cratonic shields, T_e should be assessed using the free-air admittance.

[64] There are several problems in this argument, however. For example, erosional power is proportional to slope rather than elevation, such that erosion acts far more efficiently to remove short-wavelength variations (i.e., surface loads) than the long wavelengths of flexural response to subsurface loads. If topography could in fact be reduced to absolute level, one would no longer observe the fractal property that topographic power increases log linearly with amplitude (a property ubiquitously seen in low-relief as well as high-relief regions). Most importantly, if the topographic mass that balances a subsurface load is removed, the lithosphere must flex to achieve a new isostatic balance. This will have the effect of reducing the net subsurface load (via flexural deflection of internal density discontinuities), and so both the net load and the topography will be reduced, but not removed, unless the removal of topography continues apace until the internal mass anomalies introduced by flexure balance the original subsurface load sufficiently that a topographic response is no longer required. The resulting gravity anomaly will be dominated by differences in depth of the subsurface load versus the mass anomalies introduced by flexural response to the load plus erosion. However, at wavelengths of the flexural transition and larger, the depth attenuation due to upward continuation is not very significant, and the resulting gravity anomalies would be quite small, much smaller than are in fact observed in cratonic shield regions. We have used both Bouguer coherence and free-air ad-

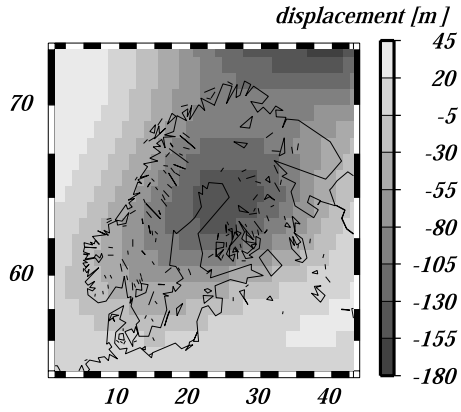

Figure 11. Surface deflections by Quaternary ice loading that have not yet been recovered by postglacial rebound (J. Wahr, personal communication, 2003). Modeling parameters consisted in a viscosity of the lower mantle of 50×10^{21} Pa s^{-1} and a lithospheric thickness of 120 km.

mittance to estimate T_e in central Finland. The two methods produce similar results with very high T_e in central Finland. This suggests that either incoherent loads do not affect T_e estimates in central Finland or that free-air admittance and Bouguer coherence are equally biased in the presence of incoherent loads.

6.2. Rheological Modeling of T_e in Central Finland

[65] Several investigators have demonstrated that continental T_e depends strongly on the thermal structure, composition, and crustal thickness of the lithosphere [*Burov and Diament*, 1995; *Lowry and Smith*, 1995]. There is now considerable information constraining the heat flow, seismic velocity structure, and thickness of the crust in Fennoscandia [*Korsman et al.*, 1999; *Kukkonen and Peltonen*, 1999; *Pasquale et al.*, 2001]. It is therefore possible to compare our estimates of T_e based on spectral modeling to predictions based on rheological models.

[66] T_e was calculated from the bending moment of the lithosphere using the leaf-spring approximation of *Burov and Diament* [1995]. The bending moment was obtained using a range of possible yield strength envelopes (YSE) and estimates of the present curvature in Finland. YSEs were constructed using a geotherm derived from mantle xenolith samples located at the border between the Svecofennian domain and the Karelian domain where the crust is 60 km thick [*Kukkonen and Peltonen*, 1999] (Figure 13). The geotherm suggests a thermal thickness of the lithosphere of at least 250 km and a temperature at the Moho of 550°C. Analysis of V_p and V_p/V_s ratios indicate that the lower crust most probably consists of mafic granulite, although possible rheologies range from anorthosite (the weakest) through mafic granulite to diabase (the strongest) (Figure 13). To simulate the range of mantle strength we used a dry (strong) and wet (weak) olivine rheology. We used observed strain rates adequate for cold, stable and relatively undeformed plate interiors in the range 3×10^{-20} s^{-1} to 1.26×10^{-17} s^{-1} [*Gordon*, 1998]. Because the yield strength of the ductile lithosphere is inversely proportional to strain rate, faster strain rates would only increase the estimates of T_e calculated here.

[67] The curvature was estimated from observations on foreland basins which provide an upper limit for curvature in Finland. Curvatures of foreland basins range from 10^{-8} m^{-1} for the sub-Andean and West Taiwan foreland basins [*Stewart and Watts*, 1997; *Lin and Watts*, 2002] to a maximum of 4 to 5 $\times$ 10^{-6} m^{-1} for the Apennine and Dinaride foreland [*Kruse and Royden*, 1994]. In Finland the curvature is likely to be smaller than that observed in foreland basins, therefore we used curvatures that range from 10^{-8} m^{-1} to 10^{-7} m^{-1}.

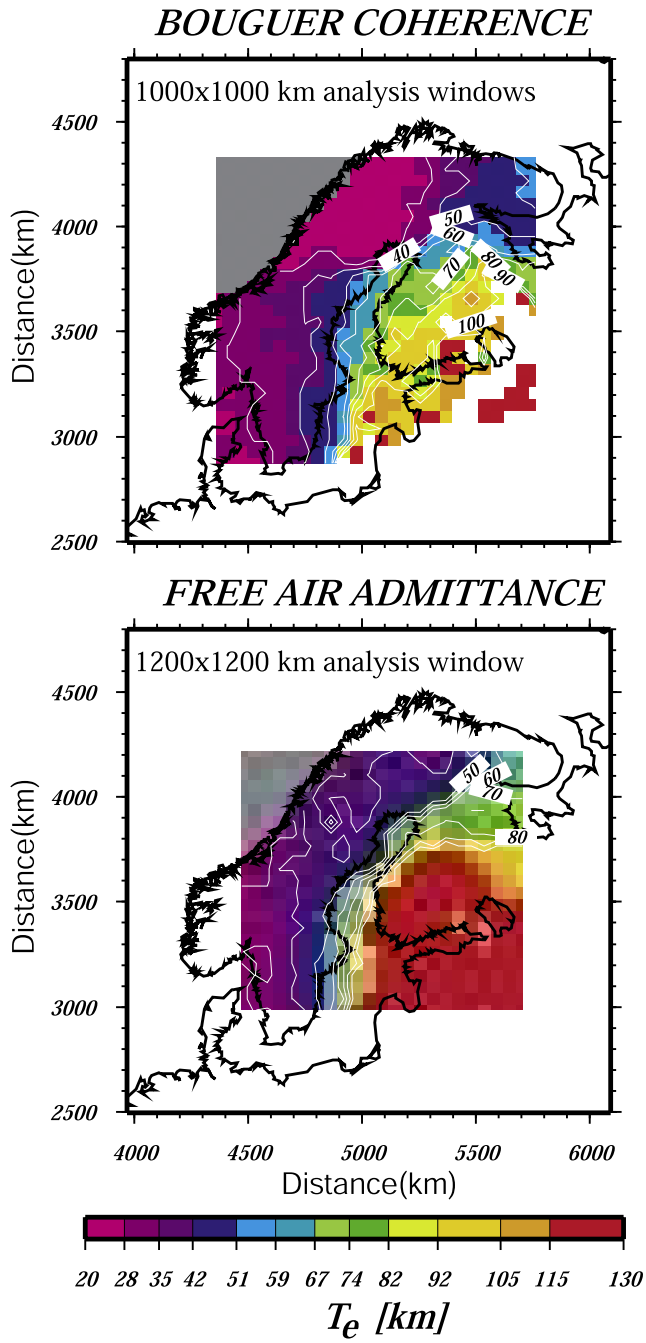

Figure 12. T_e estimates using (top) Bouguer coherence and (bottom) free-air admittance, after correcting for effects of incomplete postglacial rebound (see text).

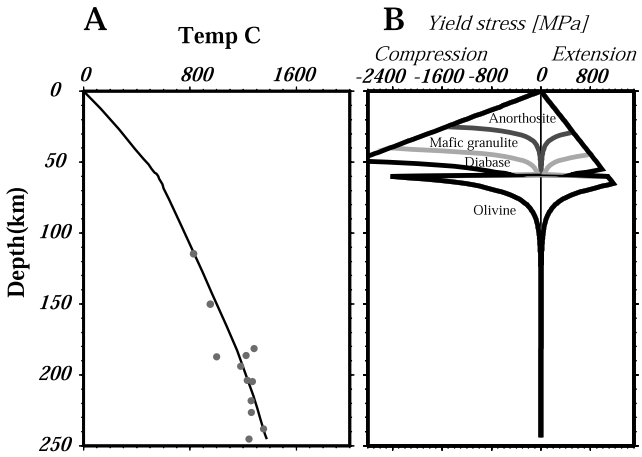

Figure 13. (a) Geotherm in central Finland, from a site located at the border between the Proterozoic Svecofennides and the Archean Karelia. The geotherm was calculated from xenolith data (gray dots) analyzed by *Kukkonen and Peltonen* [1999]. (b) Rheological profiles constructed using the geotherm shown in Figure 13a and rheologies for the lower crust corresponding to anorthosite, mafic granulite, diabase. The strain rate used in this example was 8×10^{-18} s^{-1}.

[68] Figure 14 shows the results of these calculations. If the lower crust consists of mafic granulite or diabase, T_e is independent of the crustal rheology. In these cases, the yield strength at the base of the lower crust exceeds 10 MPa, and the crust behaves as if it is coupled to the mantle [*Burov and Diament*, 1995]. If the lower crust is anorthositic, T_e is greatly reduced because the low strength at the Moho is likely to decouple the crust and mantle [*Burov and Diament*, 1995]. However, if decoupling had occurred in central Finland, the thickened lower crust there would have extruded to equilibrate the large gradient in Moho depth [e.g., *Bird*, 1991]. Therefore we consider the anorthosite case to be a lower bound, albeit an unlikely one, on T_e. Estimates of T_e using the other two lower crustal rheologies are within the range of reliable T_e estimates from Bouguer coherence and free-air admittance analysis, which indicate a T_e = 70–100 km (shaded on Figure 14).

[69] These results show that spectral methods and YSE modeling yield compatible results and that T_e in central Finland is likely to be quite high, ~70 km or more. T_e in central Finland exceeds the crustal thickness, indicating that at least some of the strength must reside in the mantle. The extreme strength of the lithosphere there appears to reflect the combined effects of a strong and cold lower crust and a high-viscosity mantle which has undergone several melting events and is therefore depleted of basaltic constituents and, importantly, volatiles [*Phipps Morgan*, 1997].

6.3. Relationship of T_e With Other Lithospheric Parameters

[70] We have calculated a detailed map of T_e in Fennoscandia. Our results are qualitatively similar to those of *Poudjom Djomani et al.* [1999]. However, we are able to estimate reliably the very high T_e of the Swedish Svecofennides and to better resolve the differences in T_e of the Proterozoic and Archean domains. There is a general correlation of increasing T_e southeastward across Fennoscandia with the decrease in heat flow and increase in seismic lithosphere thickness toward the oldest parts of the shield [*Pasquale et al.*, 2001; *Calcagnile*, 1982]. The Caledonides and coasts of Norway and southern Sweden where T_e is smallest are the areas where heat flow and seismic lithosphere thickness are lowest.

[71] However, the relationship between age, heat flow, seismic lithospheric thickness, and T_e is not unambiguous. Parts of the Archean Karelia appear to have lower T_e than the Proterozoic Svecofenides of central Finland. The relatively low T_e of the Archean Karelian province might be an artifact of the recovery. We observed in synthetic tests (Figure 4) that the area of highest estimated T_e can be smaller than the true extent of the strong cratonic core. Since the Karelian domain is surrounded by lower T_e lithosphere and the Svecofennian in central Finland is not, it is possible that T_e in the Karelian domain is biased toward lower T_e by smoothing. However, we suggest that

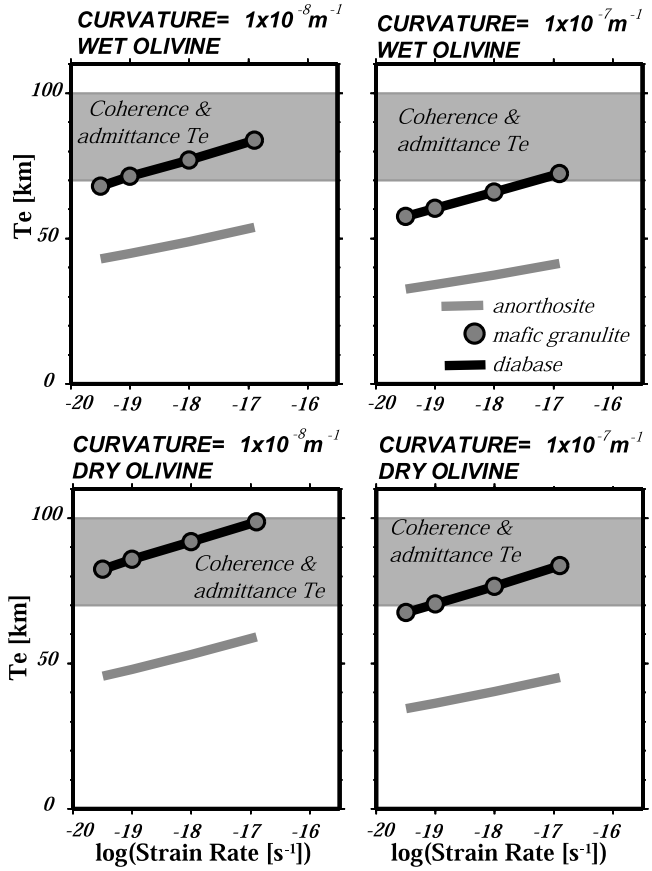

Figure 14. Estimated T_e versus strain rate using the leaf-spring approximation of *Burov and Diament* [1995]. The curvatures used are adequate for relatively undeformed continental interiors and are indicated in the diagrams. T_e was calculated assuming a range of lower crustal rheologies corresponding to anorthosite, mafic granulite, and diabase (see legend). For (top) the mantle wet and (bottom) the dry olivine rheologies were used. Gray band indicates range of T_e values obtained from Bouguer coherence and free-air admittance analyses.

the T_e in central Finland really is higher and that the greater strength is reflected by the thicker lower crustal layer and seismic lid in central Finland. The Colorado Plateau is another example of Proterozoic lithosphere that is apparently stronger than nearby Archean lithosphere. The Colorado Plateau was relatively undisturbed by Laramide contraction and subsequent extension, while the Archean southern Basin and Range has accommodated tectonism since the Paleozoic. On the basis of analysis of isotopic ratios of mantle xenoliths, *Lee et al.* [2001] suggest that the differences in strength have a compositional origin and result from greater basalt depletion of the Proterozoic mantle relative to the Archean mantle. *Wang and Mareschal* [1999] and *Simons and van der Hilst* [2002] similarly find that high T_e in the Archean and Proterozoic provinces of the Canadian and Australian shields, respectively, are not directly related to age and suggest that the differences in strength between these areas might be controlled by composition.

[72] Comparison of T_e in Fennoscandia with seismicity indicates that T_e is low where seismic activity is most frequent and T_e is high in areas of low seismicity. T_e in central Finland and Karelia, at 70–100 km, greatly exceeds the ~20 km maximum earthquake focal depth in these areas [*Pasquale et al.*, 2001], confirming that these two measures of strength are different. This result should be expected given that T_e is an integral of stress whereas focal depths depend on independent aspects of the frictional failure regime [*Watts and Burov*, 2003].

7. Conclusions

[73] We have performed tests with synthetic data and calculated T_e in Fennoscandia using the Bouguer coherence and free-air admittance functions. We have shown that when the loading models are the same, T_e estimates from these two functions are similar. The performance of free-air admittance is somewhat poorer than Bouguer coherence due to low power of the free-air anomaly at wavelengths of the isostatic transition and consequent sensitivity to leakage effects.

[74] For a given T_e value and load ratio the rollover of the observed multitapered admittance or coherence is biased toward shorter wavelengths than the rollover of the corresponding theoretical admittance or coherence functions. Hence T_e estimates obtained comparing observed multitapered admittance or coherence functions to theoretical functions are likely to be biased downward. When the observed multitapered admittance or coherence functions are compared to predicted functions multitapered with identical data windows, as is done here, the bias in the observed and predicted admittance is approximately the same, and the resulting T_e estimate is not significantly biased.

[75] The accuracy of T_e estimates depends critically on the window size used for analysis. Bias and variance of T_e estimates increase with decreasing window size and increasing T_e. To obtain a reliable T_e estimate, several analyses should be carried out using a variety of estimation window sizes. T_e estimation using sliding, overlapping windows can recover a T_e structure which closely approximates the true spatial variability, but window sizes must be chosen carefully to optimize the trade-off between variance and resolution.

[76] We obtain very similar estimates of T_e in the Fennoscandian shield from free-air admittance and Bouguer coherence analyses. The estimated T_e is 20–40 km in the Caledonides, 40–60 km in the Swedish Svecofennides, 40–60 km in the Kola peninsula, and 70–100 km in the southern Karelia province and Svecofennian central Finland.

[77] Dynamic effects due to ongoing postglacial rebound do not appear to affect coherence or admittance measurements. Potential noise introduced by long-term erosion and sedimentation also does not appear to affect the T_e measurements, given that T_e values obtained from free-air admittance and Bouguer coherence analysis are similar.

[78] An independent estimate of T_e using a xenolith-derived geotherm and a range of rheologies for the lower crust confirms that T_e in the Proterozoic Svecofennides of central Finland and the southern part of the Karelian domain should be high, of the order of 70–100 km. T_e in this region is greater than the thickness of the crust, indicating that the mantle must contribute significant strength to the total. Also, T_e greatly exceeds the seismogenic thickness. This result is not unexpected given that T_e is an integral of stress, whereas focal depths depend on independent aspects of the frictional failure regime.

[79] In general, T_e values in Fennoscandia increase with increasing tectonic age and seismic lid thickness and decreasing heat flow. T_e is low where seismicity is frequent and high where it is reduced. In Proterozoic and Archean lithosphere the relationship of T_e to age breaks down, indicating that compositional effects might be more important in determining the strength of stable continental lithosphere than tectonothermal age.

Appendix A: Load Deconvolution in Land and Ocean Areas

[80] Following *Forsyth* [1985] and *Lowry and Smith* [1994], we consider a thin plate with an arbitrary density profile $\rho(z)$, with density ρ_0 at the top ($z = 0$) and ρ_m at the base ($z = h$). However, we generalize here for the case of an arbitrary fluid density ρ_f at the surface. A surface load emplaced on the plate, $H_i(\mathbf{k})$, induces a deflection $W_t(\mathbf{k})$ resulting in surface topography $H_t(\mathbf{k}) = H_i(\mathbf{k}) + W_t(\mathbf{k})$. Similarly, a subsurface load, W_i, with density contrast $\Delta\rho_l$ emplaced at depth z_l induces a deflection which will produce topography equal to H_b. After deflection the topography on the density interface at the depth of subsurface loading is $W_b(\mathbf{k}) = W_i(\mathbf{k}) + H_b(\mathbf{k})$.

[81] The total surface topography, H, includes contributions H_t from surface loads and H_b from subsurface loads. Given a uniform T_e and incorporating the mass effect of ρ_f into the pressure term relating thin plate flexural responses $W_t(\mathbf{k})$ to $H_t(\mathbf{k})$ and $H_b(\mathbf{k})$ to $W_b(\mathbf{k})$, the total topography can be written as

$$H(\mathbf{k}) = \frac{\rho_m - \rho_0 + \frac{D}{g}k^4}{\rho_m - \rho_f + \frac{D}{g}k^4} H_i(\mathbf{k}) - \frac{\Delta\rho_l}{\rho_m - \rho_f + \frac{D}{g}k^4} W_i(\mathbf{k}). \quad \text{(A1)}$$

The total Bouguer anomaly, B, has contributions from the gravity anomaly caused by the deflection of density

interfaces due to surface loads, $2\pi G(\int_0^h (d\rho/dz)e^{-kz}dz)W_t(\mathbf{k})$; that due to the deflection caused by subsurface loads, $2\pi G(\int_0^h (d\rho/dz)e^{-kz}dz)H_b(\mathbf{k})$; and that resulting from the subsurface load itself, $2\pi G\Delta\rho_l e^{-kz_l}W_i(\mathbf{k})$. Hence

$$B(\mathbf{k}) = 2\pi G\left(-\frac{\left(\rho_0-\rho_f\right)\int_0^h \frac{d\rho}{dz}e^{-kz}dz}{\rho_m-\rho_f+\frac{D}{g}k^4}\right)H_i(\mathbf{k}) + 2\pi G\left(\Delta\rho_l e^{-kz_l}-\frac{\int_0^h \frac{d\rho}{dz}e^{-kz}dz}{\rho_m-\rho_f+\frac{D}{g}k^4}\right)W_i(\mathbf{k}). \quad \text{(A2)}$$

We have assumed that the free-air anomaly can be approximated to first order by $F = B + 2\pi G(\rho_0 - \rho_f)H$, i.e., that the terrain correction is negligible. Then the free-air anomaly is

$$FA(\mathbf{k}) = \frac{2\pi G(\rho_0-\rho_w)}{\rho_m-\rho_w+\frac{Dk^4}{g}}\left[-\int_0^h \frac{d\rho}{dz}e^{-kz}dz+\left(\frac{Dk^4}{g}+\rho_m-\rho_0\right)\right]H_i(\mathbf{k}) + \frac{2\pi G\Delta\rho_l}{\rho_m-\rho_f+\frac{Dk^4}{g}}\left[e^{-kz_l}\left(\rho_m-\rho_f+\frac{Dk^4}{g}\right) - \int_0^h \frac{d\rho}{dz}e^{-kz}dz-\left(\rho_0-\rho_f\right)\right]W_i(\mathbf{k}). \quad \text{(A3)}$$

[82] Equations (A1) and (A2) are solved from the observed topography and Bouguer anomaly to find $H_i(\mathbf{k})$ and $W_i(\mathbf{k})$, which are then used to calculate $H_t(\mathbf{k})$, $H_b(\mathbf{k})$, $B_t(\mathbf{k})$, and $B_b(\mathbf{k})$. These terms are used to generate the predicted Bouguer coherence using equation (4). Similarly, $H_i(\mathbf{k})$ and $W_i(\mathbf{k})$ are calculated from solution of equations (A1) and (A3) to generate $H_t(\mathbf{k})$, $H_b(\mathbf{k})$, $F_t(\mathbf{k})$, and $F_b(\mathbf{k})$, which are used to calculate the predicted free-air admittance via equation (5).

[83] In practice, to accommodate the variable surface fluid density ρ_f, we split the topography and gravity data into onshore and offshore contributions. We create two pairs of topography and gravity anomaly grids, one in which data from the offshore regions were masked and another vice versa. Load contributions were deconvolved via equations (A1)–(A3) using $\rho_f = \rho_w = 1000$ kg m^{-3} for the data in which land areas were masked and $\rho_f = 0$ for data in which ocean areas were masked. After deconvolution the amplitudes were recombined prior to windowing for estimation of T_e.

[84] **Acknowledgments.** We thank GETECH for providing the topography and gravity data used in this study. We tank Chris Swain and an anonymous reviewer for their detailed comments on the submitted manuscript which helped to improve this paper. We also thank Chris Swain for many fruitful discussions, for providing multitaper spectral estimation subroutines that were adapted for this investigation, and for some of the codes to generate synthetic data presented here, and we thank John Wahr for the various estimates of unrecovered glacial isostatic deflection used in the topographic noise analysis. We also thank Toivo Korja for generously providing a crustal map of Fennoscandia. We thank Frederik Simons for discussion of some of the issues presented in this paper. We thank the "marine lab," John Hillier, Tiago Cunha, and Tom Jordan, for discussions on topics presented here. M.P.G. thanks Ben Holtzman for further discussion. This research was funded by NERC under grant NER/A/S/2000/00454.

References

Armstrong, G., and A. B. Watts (2001), Spatial variations in T_e in the southern Appalachians, eastern United States, *J. Geophys. Res.*, *106*, 22,009–22,026.

Banks, R. J., R. L. Parker, and S. P. Huestis (1977), Isostatic compensation on a continental scale: Local versus regional mechanisms, *Geophys. J. R. Astron. Soc.*, *51*, 431–452.

Banks, R. J., S. C. Francis, and R. G. Hipkin (2001), Effects of loads in the upper crust on estimates of the elastic thickness of the lithosphere, *Geophys. J. Int.*, *145*, 291–299.

Bechtel, T. D., D. W. Forsyth, and C. W. Swain (1987), Mechanisms of isostatic compensation in the vicinity of the east African Rift, *Geophys. J. R. Astron. Soc.*, *90*, 445–465.

Bechtel, T. D., D. W. Forsyth, V. L. Sharpton, and R. A. F. Grieve (1989), Variations in the effective elastic thickness of the North American lithosphere, *Nature*, *343*, 636–638.

Bird, P. (1991), Lateral extrusion of lower crust from under high topography, in the isostatic limit, *J. Geophys. Res.*, *96*, 10,275–10,286.

Brace, W. F., and D. L. Kohlstedt (1980), Limits on lithospheric stress imposed by laboratory experiments, *J. Geophys. Res.*, *85*, 6248–6252.

Brown, C. D., and R. J. Phillips (2000), Crust-mantle decoupling by flexure of continental lithosphere, *J. Geophys. Res.*, *105*, 13,221–13,238.

Burov, E., and M. Diament (1995), The effective elastic thickness (T_e) of continental lithosphere: What does it really mean?, *J. Geophys. Res.*, *100*, 3905–3927.

Burov, E., M. G. Kogan, H. Lyon-Caen, and P. Molnar (1990), Gravity anomalies, the deep structure, and dynamic processes beneath the Tien Shan, *Earth Planet. Sci. Lett.*, *96*, 367–383.

Calcagnile, G. (1982), The lithosphere-asthenosphere system in Fennoscandia, *Tectonophysics*, *90*, 19–35.

Chen, W. P., and P. Molnar (1983), Focal depths of intracontinental earthquakes and their implication for the thermal and mechanical properties of the lithosphere, *J. Geophys. Res.*, *88*, 4183–4214.

Fjeldskaar, W. (1997), Flexural rigidity of Fennoscandian uplift inferred from the postglacial uplift, *Tectonics*, *16*, 596–608.

Forsyth, D. W. (1985), Subsurface loading estimates of the flexural rigidity of continental lithosphere, *J. Geophys. Res.*, *90*, 12,623–12,632.

Gaal, G., and R. Gorbatschev (1987), An outline of the Precambrian evolution of Baltic Shield, *Precambrian Res.*, *35*, 15–52.

Goetze, C., and B. Evans (1979), Stress and temperature in the bending lithosphere as constrained by experimental rock mechanics, *Geophys. J. R. Astron. Soc.*, *59*, 463–478.

Gordon, R. G. (1998), The plate tectonic approximation: Plate nonrigidity, diffuse plate boundaries, and global plate reconstructions, *Annu. Rev. Earth Planet. Sci.*, *26*, 615–642.

Gunn, R. (1943), A quantitative evaluation of the influence of the lithosphere on the anomalies of gravity, *J. Franklin. Inst.*, *236*, 47–65.

Hartley, R., A. B. Watts, and J. Fairhead (1996), Isostasy of Africa, *Earth Planet. Sci. Lett.*, *137*, 1–18.

Hjelt, S. E., and J. S. Daly (1991), SVEKALAPKO, evolution of paleoproterozoic and Archean lithosphere, in *Lithospheric Dynamics: Origin and Evolution of Continents*, p. 138, EUROPROBE Secr., Uppsala Univ., Uppsala.

Jackson, J. (2002), Strength of the continental lithosphere: Time to abandon the jelly sandwich?, *GSA Today*, *12*(9), 4–10.

Kogan, M. K., J. D. Fairhead, G. Balmino, and E. L. Makedonski (1994), Tectonic fabric and lithospheric strength of northern Eurasia based on gravity data, *Geophys. Res. Lett.*, *21*, 2653–2656.

Korsman, K., T. Korja, M. Pajunen, P. Virransalo, and G. W. Group (1999), The GGT/SVEKA Transect: Structure and evolution of the continental crust in the paleoproterozoic Svecofennian Orogen in Finland, *Int. Geol. Rev.*, *41*, 1287–1333.

Kruse, S. E., and L. H. Royden (1994), Bending and unbending of an elastic lithosphere: The Cenozoic history of the Apennine and Dinaride foredeep basins, *Tectonics*, *13*, 278–302.

Kukkonen, I. T., and P. Peltonen (1999), Xenolith-controlled geotherm for the central Fennoscandian Shield: implications for lithosphere-asthenosphere relations, *Tectonophysics*, *304*, 301–315.

Lambeck, K., P. Johnston, and M. Nakada (1990), Holocene glacial rebound and sea level change in NW Europe, *Geophys. J. Int.*, *103*, 451–468.

Lavier, L. L., and M. S. Steckler (1997), The effect of sedimentary cover on the flexural strength of continental lithosphere, *Nature*, *389*, 476–479.

Lee, C. T., Q. Yu, R. L. Rudnick, and S. T. Jacobsen (2001), Preservation of ancient and fertile lithospheric mantle beneath the southwestern United States, *Nature*, *411*, 69–73.

Lin, A. T., and A. B. Watts (2002), Origin of the West Taiwan basin by orogenic loading and flexure of a rifted continental margin, *J. Geophys. Res.*, *107*(B9), 2185, doi:10.1029/2001JB000669.

Lowry, A. R., and R. B. Smith (1994), Flexural rigidity of the Basin and Range-Colorado Plateau-Rocky Mountain transition from coherence analysis of gravity and topography, *J. Geophys. Res.*, *99*, 20,123–20,140.

Lowry, A. R., and R. B. Smith (1995), Strength and rheology of the western U.S. Cordillera, *J. Geophys. Res.*, *100*, 17,947–17,963.

Lowry, A. R., and S. Zhong (2003), Surface versus internal loading of the Tharsis rise, Mars, *J. Geophys. Res.*, *108*(E9), 5099, doi:10.1029/2003JE002111.

Macario, A., A. Malinverno, and W. F. Haxby (1995), On the robustness of elastic thickness estimates obtained using the coherence method, *J. Geophys. Res.*, *100*, 15,163–15,172.

Maggi, A., J. A. Jackson, D. McKenzie, and K. Priestley (2000), Earthquake focal depths, effective elastic thickness, and the strength of the continental lithosphere, *Geology*, *28*, 495–498.

Mandelbrot, B. B. (1983), *The Fractal Geometry of Nature*, W. H. Freeman, New York.

McConnell, R. K. (1968), Viscosity of the mantle from relaxation time spectra of isostatic adjustment, *J. Geophys. Res.*, *73*, 7089–7104.

McKenzie, D. (2003), Estimating T_e in the presence of internal loads, *J. Geophys. Res.*, *108*(B9), 2438, doi:10.1029/2002JB001766.

McKenzie, D., and D. Fairhead (1997), Estimates of the effective elastic thickness of the continental lithosphere from Bouguer and free air anomalies, *J. Geophys. Res.*, *102*, 27,523–27,552.

McNutt, M. K., and R. L. Parker (1978), Isostasy in Australia and the evolution of the compensation mechanism, *Science*, *199*, 773–775.

Menke, W. (1989), *Geophysical Data Analysis: Discrete Inverse Theory*, Academic, San Diego, Calif.

Milne, G. A., J. L. Davis, J. X. Mitrovica, H.-G. Scherneck, J. M. Johnasson, M. Vermeer, and H. Koivula (2001), Space-gteodetic constraints on Galcial isostatic adjustment in Fennoscnadia, *Science*, *291*, 2381–2385.

Mitrovica, J., and W. R. Peltier (1993), The inference of mantle viscosity from an inversion of Fennoscandian relaxation spectrum, *Geophys. J. Int.*, *114*, 45–62.

Ojeda, G. Y., and D. Whitman (2002), Effect of windowing on lithosphere elastic thickness estimates obtained via the coherence method: Results from northern South America, *J. Geophys. Res.*, *107*(B11), 2275, doi:10.1029/2000JB000114.

Parker, R. L. (1972), The rapid calculation of potential anomalies, *Geophys. J. R. Astron. Soc.*, *31*, 447–455.

Pasquale, V., M. Verdoya, and P. Chiozzi (2001), Heat flux and seismicity in the Fennoscandian Shield, *Phys. Earth Planet. Inter.*, *126*, 147–162.

Peitgen, H., and D. Saupe (1988), *The Science of Fractal Images*, 312 pp., Springer-Verlag, New York.

Percival, D. B., and A. T. Walden (1993), *Spectral Analysis for Physical Applications, Multitaper and Conventional Univariate Techniques*, pp. 1–19, Cambridge Univ. Press, New York.

Petit, C., and C. Ebinger (2000), Gravity models of the East African and Baikal rifts, *J. Geophys. Res.*, *105*, 19,151–19,162.

Phipps Morgan, J. P. (1997), The generation of a compositional lithosphere by mid-ocean ridge melting and its effect on subsequent off-axis upwelling and melting, *Earth Planet. Sci. Lett.*, *146*, 213–232.

Poudjom Djomani, Y. H., J. D. Fairhead, and W. L. Griffin (1999), The flexural rigidity of Fennoscandia: Reflection of the tectonothermal age of the lithospheric mantle, *Earth Planet. Sci. Lett.*, *174*, 139–154.

Sandoval, S., E. Kissling, and J. Ansorge (2003), High-resolution body wave tomography beneath the SVEKALAPKO array: I. A priori three-dimensional crustal model and associated traveltime effects on teleseismic wave fronts, *Geophys. J. Int.*, *153*, 75–87.

Simons, F. J., and R. D. van der Hilst (2002), Age-dependent seismic thickness and mechanical strength of the Australian lithosphere, *Geophys. Res. Lett.*, *29*(11), 1529, doi:10.1029/2002GL014962.

Simons, F. J., M. T. Zuber, and J. Korenaga (2000), Isostatic response of the Australian lithosphere: Estimation of effective elastic thickness and anisotropy using multitaper spectral analysis, *J. Geophys. Res.*, *105*, 19,163–19,184.

Simons, F. J., R. D. van der Hilst, and M. T. Zuber (2003), Spatiospectral localization of isostatic coherence anisotropy in Australia and its relation to seismic anisotropy: Implications for lithospheric deformation, *J. Geophys. Res.*, *108*(B5), 2250, doi:10.1029/2001JB000704.

Slepian, D. (1978), Prolate spheroidal wave functions, Fourier analysis and uncertainty, V, The discrete case, *Bell. Syst. Tech. J.*, *57*, 1031–1042.

Stark, C. P., J. Stewart, and C. J. Ebinger (2003), Wavelet transform mapping of effective elastic thickness and plate loading: Validation using synthetic data and application to the study of southern African tectonics, *J. Geophys. Res.*, *108*(B12), 2558, doi:10.1029/2001JB000609.

Stewart, J. (1998), Gravity anomalies and lithospheric flexure: Implications for the thermal and mechanical evolution of the continental lithosphere, Ph.D. thesis, Oxford Univ., Oxford, U.K.

Stewart, J., and A. B. Watts (1997), Gravity anomalies and spatial variations of flexural rigidity at mountain ranges, *J. Geophys. Res.*, *102*, 5327–5352.

Swain, C. J., and J. F. Kirby (2003a), The effect of "noise" on estimates of the elastic thickness of the continental lithosphere by the coherence method, *Geophys. Res. Lett.*, *30*(11), 1574, doi:10.1029/2003GL017070.

Swain, C. J., and J. F. Kirby (2003b), The coherence method using a thin anisotropic elastic plate model, *Geophys. Res. Lett.*, *30*(19), 2014, doi:10.1029/2003GL018350.

Thomson, D. J. (1982), Spectrum estimation and harmonic analysis, *Proc. IEEE*, *70*, 1055–1096.

Thomson, D. J., and A. D. Chave (1991), Jackknifed error estimates for spectra, coherences, and transfer functions, in *Advances in Spectrum Analysis and Array Processing*, edited by S. Haykin, pp. 58–113, Prentice-Hall, Old Tappan, N. J.

Turcotte, D. (1997), *Fractals and Chaos in Geology and Geophysics*, Cambridge Univ. Press, New York.

Walden, A. T. (1990), Maximum Likelihood estimation of magnitude-squared multiple and ordinary coherence, *Signal Processes*, *19*(1), 75–82.

Walden, A. T., E. J. McCoy, and D. B. Percival (1995), The effective bandwidth of a multitaper spectral estimator, *Biometrika*, *82*(1), 201–214.

Wang, Y., and J. Mareschal (1999), Elastic thickness of the lithosphere in the central Canadian Shield, *Geophys. Res. Lett.*, *26*, 3033–3036.

Watts, A. B. (1978), An analysis of isostasy in the world's oceans: 1. Hawaiian-Emperor seamount chain, *J. Geophys. Res.*, *83*, 5989–6004.

Watts, A. B. (2001), *Isostasy and Flexure of the Lithosphere*, Cambridge Univ. Press, New York.

Watts, A. B., and E. Burov (2003), Lithospheric strength and its relationship to the elastic and seismogenic layer thickness, *Earth Planet. Sci. Lett.*, *213*, 113–131.

Watts, A. B., and S. Zhong (2000), Observations of flexure and the rheology of the oceanic lithosphere, *Geophys. J. Int.*, *142*, 855–875.

Watts, A. B., J. H. Bodine, and M. S. Steckler (1980), Observations of flexure and the state of stress in the oceanic lithosphere, *J. Geophys. Res.*, *85*, 6369–6376.

Willett, S. D., D. S. Chapman, and H. J. Neugebauer (1984), Mechanical response of the continental lithosphere to loading: Effect of thermal regimes, *Ann. Geophys.*, *2*, 679–688.

Willett, S. D., D. S. Chapman, and H. J. Neugebauer (1985), A thermomechanical model of continental lithosphere, *Nature*, *314*, 520–523.

Windley, B. (1993), Proterozoic anorogenic magmatism and its orogenic connections, *J. Geol. Soc. London*, *150*, 39–50.

Wolf, D. (1987), An upper bound on the lithosphere thickness from glacio-isostatic adjustment in Fennoscandia, *J. Geophys. Res.*, *61*, 141–149.

Wyer, P. (2003), Statistical studies of seafloor geomorphology, Ph.D. thesis, Oxford Univ., Oxford, U.K.

A. R. Lowry and I. Velicogna, Department of Physics, University of Colorado, Campus Box 390, Boulder, CO 80309, USA. (arlowry@himalaya.colorado.edu; isabella@colorado.edu)

M. Pérez-Gussinyé and A. B. Watts, Department of Earth Sciences, Oxford University, Parks Road, Oxford OX1 3PR, UK. (marta@earth.ox.ac.uk; tony@earth.ox.ac.uk)